2019

Additive manufacturing of flexible energy harvesting and storage device

Bolin Chen
Iowa State University

Additive manufacturing of flexible energy harvesting and storage device

by

Bolin Chen

A dissertation submitted to the graduate faculty

in partial fulfillment of the requirements for the degree of

DOCTOR OF PHILOSOPHY

Major: Mechanical Engineering

Program of Study Committee:
Jonathan Claussen, Co-major Professor
Shan Hu, Co-major Professor
Xinwei Wang
Yue Wu
Richard Stone

The student author, whose presentation of the scholarship herein was approved by the program of study committee, is solely responsible for the content of this dissertation. The Graduate College will ensure this dissertation is globally accessible and will not permit alterations after a degree is conferred.

Iowa State University

Ames, Iowa

2019

DEDICATION

In dedication to Dad, Mom and my mentors for supporting and understanding me all the way.

TABLE OF CONTENTS

Page

ACKNOWLEDGMENTS

I would like to thank my committee chair, Dr. Jonathan Claussen, Dr. Shan Hu and my committee members, Dr. Xinwei Wang, Dr. Yue Wu, Dr. Richard Stone for their guidance and support throughout the course of this research.

In addition, I would also like to thank my friends, colleagues, the department faculty and staff for making my time at Iowa State University a wonderful experience. I want to also offer my appreciation to those who were willing to participate in my surveys and observations, without whom, this thesis would not have been possible.

ABSTRACT

Printing technology as an additive manufacturing method offers promising approach to deposit functional nanomaterials in a scalable fashion. Thermoelectric generators (TEGs) offer seemingly limitless, clean energy to power ever more increasing and complex wearable and pocket devices. The burgeoning field of wearable technologies, or body worn application-enabled computing devices, are capable of providing user feedback/alerts from multiple devices that continuously monitor metrics such as physical and muscular activity; cardiac and respiratory rates; as well as temperature, humidity, and light. The challenge of supplying continuous power in a non-invasive fashion to ever more complex and numerous wearable devices is a key prohibitive bottleneck to commercialization. A manufacturing process involved additive manufacturing is studied to highly-efficient thermoelectric generators to power wearable devices via body heat.

Such wearable power generation would be of interest to a myriad of applications including those associated with particular fields of work/leisure efficiency (e.g., computing and communication devices that connect to the internet and supply requested information), biomedical monitoring (e.g., wearable sensors that monitor respiratory, muscular, and metabolism activity) and military applications (e.g., devices that alert the warfighter of nearby biochemical threats).

On the other hand, supercapacitors have emerged as a promising energy storage device, due to their high power, long cycle life, and ability to bridge the energy and power gap between batteries and conventional dielectric capacitors. Supercapacitors are widely used in electronic systems where fast and frequent charging/discharging is required. Hybrid power sources integrating batteries and supercapacitors together provide both high energy and high power at the

same time. Herein, we report for the first time the use of DIW technology for printing fully packaged flexible supercapacitors.

CHAPTER 1. INTRODUCTION

1.1 Introduction

1.1.1 Thermoelectricity

The global energy consumption is increasing each year as reported by the international energy agency[1]. Just look at the United States in 2019, traditional energy source such as petroleum, natural gas and coal are still the dominant energy sources. Not all the energy is used as Energy service, more than 60 % of the energy are ejected as waste. Most of them are in the form of heat. The global oil price is fluctuating and there is an increasing concern about the greenhouse gases. Newer technologies are been developed to make the use of energy more efficient. For example, more efficient engine, solar cell, etc. Therefore, it is important to develop highly efficient thermoelectric generator (TEG) for waste-heat recovery. Highly efficient thermoelectric materials are important for usable thermoelectric energy recovery that convert heat into electrical energy. The conversion of heat into electricity plays a key role in our current challenge to develop alternative energy technologies to reduce greenhouse gas emission. Mobile charge carriers (electrons or holes) at the hot side of the material have more thermal energy than carriers at the cold side, causing a net diffusion of mobile carriers to the cold side. Since there are more mobile carriers at the cold side than the hot side, the inhomogeneous charge distribution forms an electric field which opposes the diffusion. Bi_2Te_3-based thermoelectric material have been developed in the 1950s and are promising materials for waste heat recovery and power generation near room temperature (RT) (~300 K). These alloys originally exhibit good thermoelectric characteristics such as high carrier mobilities and low lattice thermal conductivities. Bismuth antimony telluride ($(Bi_{1-x}Sb_x)_2Te_3$) (p-type) and bismuth selenium telluride ($Bi_2(Se_{1-x}Te_x)_3$) (n-type) are the most common combination for RT TEG. In general, the

thermoelectric performance of a material is evaluated by the dimensionless figure of merit, $ZT = \sigma S^2 T/\kappa$, where σ is the electrical conductivity, S is the Seebeck coefficient, T is the absolute temperature, and κ is the thermal conductivity. This material system is the only thermoelectric material system whose ZT is larger than 1.0 near room temperature so far.

1.1.2 Solar To Thermal Conversion

An alternative way to harvest wasted thermal energy is by harvesting solar irradiation. Solar thermal energy is a technology for harvest solar irradiation to generate thermal energy or electrical energy. Different approaches has been implemented to harvest solar thermal energy, such as concentrated solar power plant[2] in Nevada, vacuum tube solar water heater that been wildly used in China[3]. Also, there are some innovative highly efficient composite contains nanomaterials in the research stage[4,5].

A solar thermal conversion system generally consists of two essential components, i.e., solar collectors that convert solar irradiation into thermal energy and thermal energy storage (TES) materials that store and later release the converted thermal energy for various useful purposes. It is desirable for the solar collector to be a black color for absorbing light across a wide wavelength range. Excellent heat transfer from the solar collector to the TES material is also necessary to prevent the overheating of the collector. To this end, in existing solar thermal conversion systems, the passages that carry the TES are usually embedded into the solar absorber plate to ensure good thermal conduct between the absorber plate and the TES[6].

1.1.3 Printed flexible supercapacitor

The ability to print fully packaged integrated energy storage components (e.g., supercapacitors) is of critical importance for practical applications of printed electronics. Due to the limited variety of printable materials, most studies on printed supercapacitors focus on printing the electrode materials but rarely the full-packaged cell. This work presents for the first

time the printing of a fully packaged single-wall carbon nanotube-based supercapacitor with direct ink writing (DIW) technology. Enabled by the developed ink formula, DIW setup, and cell architecture, the whole printing process is mask free, transfer free, and alignment free with precise and repeatable control on the spatial distribution of all constituent materials.

1.2 Introduction to different printing technique

1.2.1 Screen printing

Screen printing is one of the commercially used printing technique to produce thick film with a given pattern. It has multiple drawbacks including low line resolution (>100 μm), material waste as material becomes adhered to the squeegee in lieu of being printed, and higher prototyping costs as a new stencil or mask is needed for each new design. Dispenser printing also has drawbacks such as the necessity to use viscous pastes (≈100—10 000 cP for dispenser printing vs 5 – 15 cP for inkjet printing) that require the use of additive materials (e.g., poly(3-hexyl thiophene)) and controlling the height and temperature of the dispenser needle while preventing breakage and contamination are all challenging the printing efficiency as well as overall cost. Functional devices contain advanced nanomaterials are commonly produce by nanofabrication technique, which suffered from the low throughput and costly clean room facilities.

1.2.2 Direct ink writing

The term direct ink writing (DIW) describes fabrication methods that employ a computer-controlled printing stage with moves a pattern generating device, that is an ink-deposition nozzle, to create materials with controlled architecture and composition[7]. Several direct ink writing techniques have been introduced that capable of patterning materials in 2D or 3D. They can be divided into filamentary-based approaches, such as robocasting, micropen writing, and fused

deposition and droplet based such as inkjet printing. Idela materilas for DIW should have viscoelastic property that can be easily tuned such as Colloidal gels. They should flow through the deposition nozzle and then “set” immediately to facilitate shape retention of the deposited features even as they span gaps in the underlying layer(s). Also it they must contain a high colloid volume fraction to minimize drying-induced shrinkage after assembly is complete, so the particle network is able to resist compressive stresses arising from capillary tension[8].

1.2.3 Inkjet printing

The thin-film methods provided several favorable features compared to the bulk methods. For example, it is possible to reduce the device size and manufacturing cost. In addition, the thin-film technology can easily incorporate nanoscale effects such as a reduction in thermal conductivity due to phonon scattering and increase in Seebeck coefficient due to the reduced dimensions. The structural and thermoelectric properties of the thin films differ according to the deposition method. In this regard, various studies have been performed on crystal materials (single-crystal, polycrystal), powdered sintered materials (cold-press sintered, hot-pressed, spark plasma sintered), thin-film materials, etc. In the later chapter, a scable manufacturing method called inkjet printing is used to fabricate flexible TEG and performance is tested on a prototype.

1.3 Nanoscale effect

Nanostructured materials give unique properties which cannot be achieved on bulk, such as high surface area, improved electrical/ thermal transport. The present interest in low-dimensional thermoelectric materials was promoted by the thermotical work of Hicks and Dresselhaus[9]. Their calculations were based on a conductor with a single parabolic band was used in the theory, but the valence band would have suited the purpose equally well. They first obtained an expression for the dimensionless figure of merit in the 3-D case in terms of the

Fermi energy and a parameter that is virtually the same as Chasmar and Stratton's β, modified to allow for anisotropy of the effective mass.

There have been a number of experimental demonstrations of imported figure of merit in nanostructured TE materials. Even when the electronic properties do not change, zT can still be larger than for bulk materials, This is associated with the reduction of lattice thermal conductivity due to the stronger phonon scattering when the size of sample in at least one direction is reduced[10,11].

1.4 Research objective

The long-term goal is to develop wearable TEGs that are capable of converting body heat to sufficient power to operate wearable electronic devices and develop wearable energy storage system (supercapacitor). The specified objectives for each project are as follows:

To evaluate whether proposed materials are suitable for printing technique and shows high performance once the device is completed.

To optimize the diverse manufacturing methodologies needed to create efficient, flexible and biocompatible TE networks that can interface and conform to the human body to test whether the fabrication process is scalable and low cost to produce high performance device.

1.5 Dissertation Overview

In chapter 1, a general introduction to the research is presented, which includes some major concepts related to printed flexible energy harvester and storage device. This dissertation contains four projects that are detailed presented in chapter 2-5. The first project (chapter 2-3) introduces a new approach to fabricate thermoelectric nanowire onto plane substrate by inkjet printing formulated nanowire ink. Solution phase printing of nanomaterials is becoming increasingly important for the creation of scalable flexible electronics including those associated with biomedical and energy harvesting applications. However, the use of solution-phase printed

thermoelectric energy generators (TEGs) has been minimally explored. Herein we report a highly flexible inkjet-printed TEG. Bismuth telluride (Bi2Te3) and bismuth antimony telluride (Bi0.5Sb1.5Te3) nanowires (NWs) are inkjet printed onto polyimide to form n-type and p-type legs for the TEGs. A post-print thermal annealing process is used to increase the thermoelectric performance of the printed NWs while eutectic gallium–indium (EGaIn) liquid metal contacts electrically connect the TEG legs in series. Annealing conditions for the combination of p/n legs are examined to maximize the thermoelectric efficiency of the TEG prototype[12,13].

In the second project (chapter 4), the use of DIW technology for printing fully packaged flexible supercapacitors is been reported. All components of the supercapacitor are directly written on a flexible polyimide substrate, including single-wall carbon nanotube (SW-CNT) electrode, poly(vinyl alcohol) (PVA)- based gel electrolyte, and silicone for cell packaging and sealing. SW-CNT is used as the model electrode material in this study because it has high electrical conductivity, mechanical strength, as well as high specific surface area that is open to surface functionalization for enhanced energy storage performance. PVA can form flexible and quasi-solid-state electrolyte when mixed with a variety of aqueous electrolyte solution, such as sulfuric acid (H2SO4), phosphoric acid (H3PO4), lithium chloride (LiCl), potassium hydroxide, etc. Here, the PVA− LiCl system is chosen as the model electrolyte for its neutral and benign nature. The entire printing process is assembly free, transfer free, and mask free. DIW controls the spatial distribution of printed materials with high accuracy and repeatability, which is demonstrated by the printing of multiple highly symmetric supercapacitors connected in series[14].

In the third project (chapter 5), a matrix material from carbonized wood will be utilized for the first time to develop a novel phase change material (PCM) composite. Specifically, the proposed PCM composite consists of carbonized wood (CW) monolithic infiltrated with organic PCM and sealed with graphite coating, which closely mimics the solar collector design in existing solar thermal systems. Thermal property characterization of the as-synthesized n-octadecane/CW composite shows that compared with pristine n-octadecane the composite demonstrates a 143% increase of thermal conductivity with no significant reduction in latent heat. The composite also efficiently absorbs solar light and converts it into thermal energy with an apparent 97% solar-to-thermal conversion efficiency[6].

In the last chapter, chapter 6, a general conclusion of the research works is presented and recommendation for the future work are suggested.

1.6 References

1. Statistics | World - Total Primary Energy Supply (TPES) by source (chart) Available online: https://www.iea.org/statistics/?country=WORLD&year=2016&category=Energy supply&indicator=TPESbySource&mode=chart&dataTable=BALANCES (accessed on Jul 25, 2019).

2. Zhang, H.L.; Baeyens, J.; Degrève, J.; Cacères, G. Concentrated solar power plants: Review and design methodology. *Renew. Sustain. Energy Rev.* **2013**, *22*, 466–481.

3. Morrison, G.L.; Budihardjo, I.; Behnia, M. Water-in-glass evacuated tube solar water heaters. *Sol. Energy* **2004**, *76*, 135–140.

4. Cooper, T.A.; Zandavi, S.H.; Ni, G.W.; Tsurimaki, Y.; Huang, Y.; Boriskina, S. V.; Chen, G. Contactless steam generation and superheating under one sun illumination. *Nat. Commun.* **2018**, *9*, 5086.

5. Yang, Y.; Zhao, R.; Zhang, T.; Zhao, K.; Xiao, P.; Ma, Y.; Ajayan, P.M.; Shi, G.; Chen, Y. Graphene-Based Standalone Solar Energy Converter for Water Desalination and Purification. *ACS Nano* **2018**, acsnano.7b08196.

6. Chen, B.; Han, M.; Zhang, B.; Ouyang, G.; Shafei, B.; Wang, X.; Hu, S.; Chen, B.; Han, M.; Zhang, B.; et al. Efficient Solar-to-Thermal Energy Conversion and Storage with High-Thermal-Conductivity and Form-Stabilized Phase Change Composite Based on Wood-Derived Scaffolds. *Energies* **2019**, *12*, 1283.

7. Lewis, J.A. Direct Ink Writing of 3D Functional Materials. *Adv. Funct. Mater.* **2006**, *16*, 2193–2204.

8. Guo, J.J.; Lewis, J.A. Aggregation Effects on the Compressive Flow Properties and Drying Behavior of Colloidal Silica Suspensions. *J. Am. Ceram. Soc.* **1999**, *82*, 2345–2358.

9. Hicks, L.D.; Dresselhaus, M.S. Thermoelectric figure of merit of a one-dimensional conductor. *Phys. Rev. B* **1993**, *47*, 16631–16634.

10. Lin, Y.-M.; Dresselhaus, M.S. Thermoelectric properties of superlattice nanowires. *Phys. Rev. B* **2003**, *68*, 075304.

11. Minnich, A.J.; Dresselhaus, M.S.; Ren, Z.F.; Chen, G. Bulk nanostructured thermoelectric materials: Current research and future prospects. *Energy Environ. Sci.* 2009, *2*, 466–479.

12. Chen, B.; Kruse, M.; Xu, B.; Tutika, R.; Zheng, W.; Bartlett, M.D.; Wu, Y.; Claussen, J.C. Flexible thermoelectric generators with inkjet-printed bismuth telluride nanowires and liquid metal contacts. *Nanoscale* **2018**, *11*, 5222–5230.

13. Chen, B.; Das, S.R.; Zheng, W.; Zhu, B.; Xu, B.; Hong, S.; Sun, C.; Wang, X.; Wu, Y.; Claussen, J.C. Inkjet Printing of Single-Crystalline Bi 2 Te 3 Thermoelectric Nanowire Networks. *Adv. Electron. Mater.* **2017**, *3*, 1600524.

14. Chen, B.; Jiang, Y.; Tang, X.; Pan, Y.; Hu, S. Fully Packaged Carbon Nanotube Supercapacitors by Direct Ink Writing on Flexible Substrates. **2017**.

CHAPTER 2. INKJET PRINTING OF SINGLE-CRYSTALLINE Bi_2Te_3 THERMOELECTRIC NANOWIRE NETWORKS

This chapter is modified from a paper published in "*Adv. Electron. Mater.* 2017, 3, 1600524."

*Bolin Chen, Suprem R. Das, Wei Zheng, Bowen Zhu, Biao Xu, Sungbum Hong, Chenghan Sun, Xinwei Wang, Yue Wu and Jonathan C. Claussen**

Bolin Chen, Suprem R. Das, Bowen Zhu, Prof. Xinwei Wang, Prof. J. C. Claussen
Mechanical Engineering, Iowa State University, Ames IA 50011, USA
*Corresponding Author E-mail: jcclauss@iastate.edu

Wei Zheng, Biao Xu, Sungbum Hong, Chenghan Sun, Prof. Yue Wu
Chemical and Biological Engineering, Iowa State University, Ames IA 50011, USA

2.1 Abstract

Large-scale and low-cost fabrication techniques are needed to commercialize highly efficient, nanomaterial-based thermoelectric generators (TEGs) for use in small-scale, flexible applications (e.g., wearable energy harvesters). Herein we present the first demonstration of inkjet printed networks of phase-pure, single crystalline Bi_2Te_3 thermoelectric nanowires (BTNWs) that are amenable to large scale production. The BTNWs are synthesized via chemical batch processing and formulated into a jettable ink that is printed onto glass substrates and subsequently annealed in nitrogen and forming gas environments. The inkjet-printed BTNWs annealed in forming gas provide the most favorable results with comparable thermoelectric performances to bulk Bi_2Te_3 materials (Seebeck coefficient > 100 $\mu V\ K^{-1}$) while approximately utilizing only 1% to 3% of the telluride materials found in their bulk counterparts. Thus, these printed BTNWs help pave the way for the development of low-cost, and scalable TEGs.

2.2 Introduction

Thermoelectric generators (TEGs), solid state devices that convert heat into electricity, have been in use for over 35 years in primarily large-scale applications such as power plants and

space exploration equipment (*e.g.*, NASA's space probe Voyager).[1, 2] Recent efforts to increase the efficiency of thermoelectric materials via nanoscale synthesis and structuring has begun to enable small-scale TEG applications including those associated with flexible and wearable platforms such as TEG embedded T-shirts and armbands.[3-5] Nanoscale bismuth chalcogenide [*e.g.*, bismuth telluride (Bi_2Te_3) its doped derivatives and bismuth selenide (Bi_2Se_3)] has shown great potential for use in small-scale TEG applications as it is among the most efficient materials for thermoelectric power generation (the figure of merit or ZT values ranging between 0.8 - 1.0 for bulk at low temperature ranges, *i.e.*, 200-400 K).[6-8] Furthermore, the synthesis of Bi_2Te_3 materials in the form of nanowires has led to further increases in ZT values due to reduced thermal conductivities pertaining to surface and boundary phonon scattering, enhanced Seebeck coefficients due to quantum confinement of carriers, and 1D carrier transport due to quantized density of states.[9-11] Thus BTNWs show tremendous promise for the development of small-scale TEGs.

Numerous techniques have been developed for incorporating BTNWs into TEGs. For example, phase pure and crystalline BTNWs (average dia. circa 30-40 nm and average length circa 500 nm, see Figure S1) have been synthesized and formed into macroscale pellets via hot-pressing techniques.[12-14] These nanowire-infused pellets display several advantages over bulk material pellets including enhanced phonon scattering due to the high degree of grain boundaries/nanowire interfaces, high electrical conductivity (423-507 Scm^{-1}), and high Seebeck coefficients (240-360 μVK^{-1})[12]. These bulk composite pellets can be further processed into millimeter-thick pillar device structures via compressing/sintering, micro-machining, and manual welding to metal interconnects—techniques that are labor intensive and require copious amounts of telluride-based nanomaterials that are expensive, scarce, and sometimes toxic. Other research groups have made

tremendous strides on improving/tuning the properties of BTNWs.[15-17] However, this research is limited to lab-scale device fabrication and measurements performed on a single nanowire, thin film of nanocrystals, or on hetero-structures with maximum dimensions of hundreds micro-meters—all techniques that are not amenable to large-scale TEG production.

Some research groups have begun to explore large-scale, thin film fabrication of TEG devices. Co-evaporator physical vapor deposition that requires two distinct boats (Bi and Te) and low pressure/vacuum environment which is costly (high power consumption to evaporate metal and maintain vacuum) and highly trained personnel to operate the equipment. Other groups have developed high-yield, low cost printing methods. For example, various printing techniques such as screen printing, and dispenser printing have been recently explored for producing TEGs in a scalable fashion.[18-21] However, screen printing has multiple drawbacks including low line resolution (> 100 μm), material waste as material becomes adhered to the squeegee in lieu of being printed, and higher prototyping costs as a new stencil or mask is needed for each new design. Dispenser printing also has drawbacks such as the necessity to use viscous pastes (approximately 100-10000 cP for dispenser printing vs 5-15 cP of inkjet prining) which requires the addition of additive materials [*e.g.*, poly(3-hexyl thiophene) (P3HT)] and dispenser needle challenges such as incorrect height, temperature, breakage, and contamination that can all reduce the printing efficiency as well as over cost.[22] Also both screen and dispenser printing produce thick films (*i.e.*, > 100 μm) which introduce a degree of parasitic resistances due to the higher number of junctions found in thicker printed materials.[23, 24] However, high resolution (< 100 μm feature size) inkjet printing that requires no mask or stencil (i.e., printer can be programmed with computer aided design software for pattern formation), and can print droplet thick lines (< 1 μm) provides an

alternative more precise and lower cost scalable printing process as shown in inkjet printed electrochemical sensors[25], transparent conductors[26], photovoltaics[27], and supercapacitors.[28]

Herein we report, for the first time, inkjet printed BTNWs without any additives/conducting elements, for scalable, TEG production. The nanowires are synthesized via solution phase processing according to our previous protocols. The nanowires are converted into jettable ink, without the use of additives such as exogenous conductive particles, and printed into films of various thicknesses. The printed BTNW films are subsequently annealed within two distinct ambient conditions (*i.e.*, nitrogen vs. forming gas ambient) to improve their thermoelectric properties—electrical conductivity, thermal diffusivity and Seebeck coefficient.

2.3 Results and Discussion

Batch synthesis of BTNWs was conducted following our previously reported chemical synthesis methods (Figure 1a & Experimental section)[12, 13]. In short, ultrathin tellurium nanowires were fabricated by dissolving and reducing a tellurium precursor [*i.e.*, tellurium dioxide (TeO_2)] along with potassium hydroxide (KOH), polyvinylpyrrolidone (PVP), and ethylene glycol (EG) within a controlled temperature (160°C) bath for 10 mins. A small injection of hydrazine hydrate (~1ml) is added to the solution to help reduce TeO_2 and form tellurium nanowires. Next bismuth precursors ($BiNO_3$) were added to the mixture to induce the formation of the final BTNWs. Note that the PVP was used in the reaction to act as a surfactant that prevents nanowire amalgamation and proper nanowire formation.

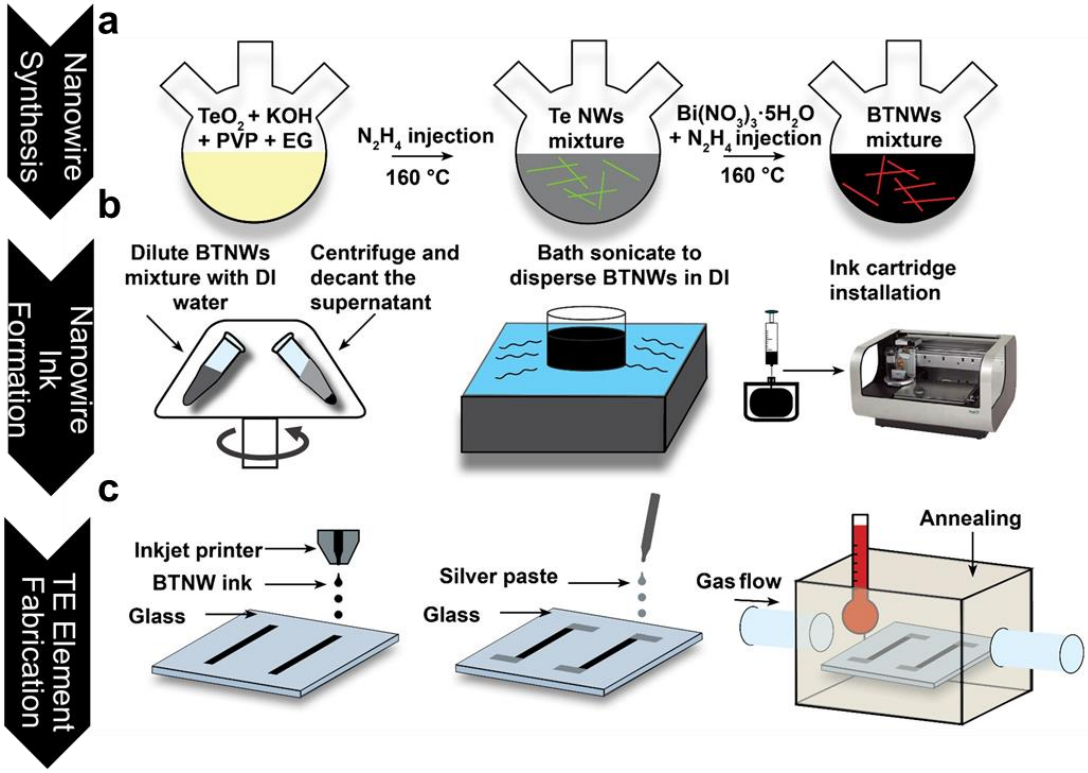

Figure 1. Schematic diagram of the nanowire synthesis, processing and printing protocols: (**a**) Two step chemical synthesis of Bi_2Te_3 nanowires (BTNWs), (**b**) BTNW ink formulation, and (**c**) inkjet printing of resultant BTNW ink and post annealing processes.

The BTNWs were next made into a jettable ink and printed onto both rigid substrates (Figure 1b-c & Experimental section). After BTNW formation, the nanowires were washed via centrifugation, redispersed in DI water with the aid of bath sonication to form a jettable ink, and finally inkjet printed onto glass substrates for testing. Both the BTNW dispersion concentration as well as the solution viscosity (10-12 cP) were tuned to prevent the piezoelectric printer nozzle from clogging. It should be noted that the average nanowire length of the BTNWs is ~ 1440 nm and average diameter is ~ 30nm, both of which are much smaller than the 1pL nozzle diameter.[12, 14] Therefore additional size reduction processing of the BTNWs, such as ball milling, was unnecessary in the ink formulation process. The number of passes that the printer head made to complete the printer process was varied (*i.e.*, 25 print layers ~ 0.4 μm thick, 50 print layers ~ 0.75 μm thick, 75 print layers ~ 1.1 μm thick, 100 print layers ~ 1.6 μm thick) and

the nozzle voltage was tuned (21-24 V) to subsequently alter the thickness of the printed BTNW layer/network and subsequently to improve its thermoelectric efficiency.

The thermoelectric properties of the printed BTNWs were also improved by using post-printing annealing processing. Various techniques, including thermal annealing, have been used to reduce the inter-particle resistance of 1D nanowire network structures comprised of a variety of materials including carbon nanotubes and silver nanowires.[29-33] In this work, we developed two distinct thermal annealing protocols for the printed BTNW networks: 1) thermal annealing in a purely nitrogen ambient and 2) thermal annealing in a forming gas ambient (*i.e.*, 95% pure dry argon gas premixed with 5% pure dry hydrogen gas). Both annealing protocols were conducted at 400°C for 2 hours followed by a cooling time in the same respective gas. Field effect scanning electron microscopy (FESEM) images of the printed BTNW networks reveal morphological changes in the nanowire nanostructure before and after the annealing processes (Figure 2). The un-annealed BTNWs retain their original 1D dimensions/morphology after the printing process with an approximate average length and width of 1.5 μm and 30 nm respectively (Figure 2a & Supporting Information). However, upon annealing in the forming gas ambient, morphological/density changes in the nanowires occur with closer nanowire packing arrangements and thicker/shorter nanowires (approximate average length and width of 130 μm and 40 nm respectively).

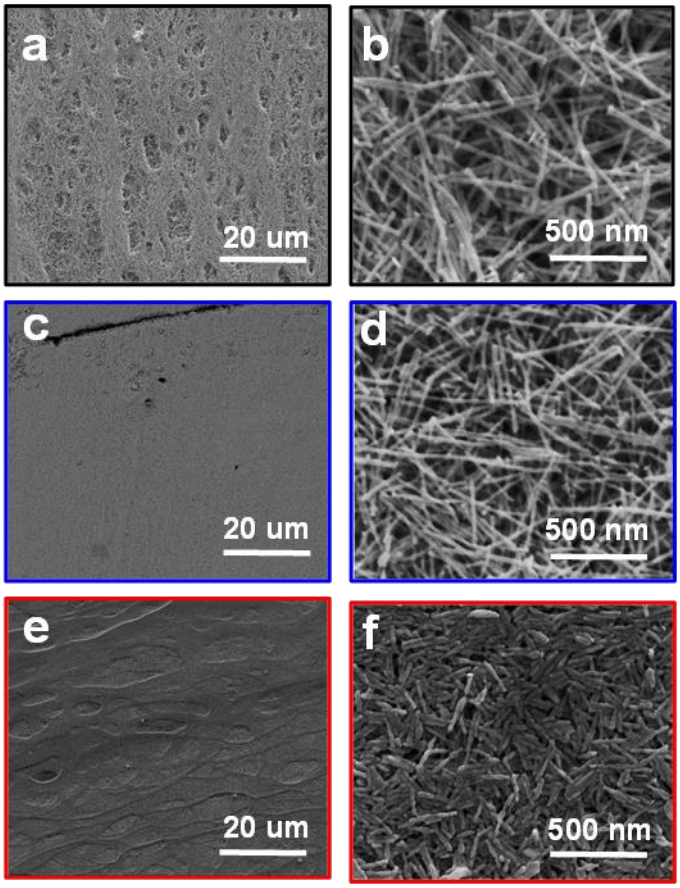

Figure 2. Low resolution (left column) and high resolution (right column) FESEM images of (**a** & **b**) un-annealed printed BTNWs nanowires, (**c** & **d**) annealed in a nitrogen gas ambient, and (**e** & **f**) annealed in a forming gas. All annealing was performed at 400°C for 1 hour of duration.

The crystal structure/phase information also varied according to the post-print BTNW annealing conditions. X-ray diffraction (XRD) measurements of un-annealed and annealed printed BTNWs revealed changes in the crystallinity as noted in the indexed XRD peaks, *i.e.*, (015), (1010), and (110) as denoted in Figure 3. These peaks correspond to the 2θ values that are consistent with Bi_2Te_3 material peaks while the sharpness of the peaks is an indicator of the crystallinity of the nanowires (*i.e.*, an increase in the sharpness of the 2θ peaks signifies an increase in the crystalline nature of the nanowires). Also, it should be noted that the broad XRD broad peak, visible between $15° < 2\theta < 40°$ on all tested samples, is indicative of the substrate peak (amorphous nature of glass) upon which the BTNWs were printed on (see glass control

XRD measurement in Figure 3). Comparison of XRD peak intensities reveals that the 2θ peaks become sharper after the printed BTNWs are annealed in a forming gas ambient as compared to BTNWs annealed in nitrogen or not annealed at all. The improved sharpness in XRD peaks in case of forming gas annealed printed nanowires is attributed to the packed microstructure of the BTNW networks which also correspond to the visible morphological changes displayed in in Figure 2 as well as the electrical and thermoelectric properties presented in the subsequent sections. However, the decreased intensity of XRD peaks in case of nitrogen annealed nanowire films might arise from the enhanced anisotropy of the network causing incoherent x-ray scattering as compared to the unannealed sample. The presence of no other peaks found in the three samples indicates the phase purity of the material and denotes a contaminant-free BTNW environment without material segregation. Furthermore, energy dispersive x-ray spectroscopy (EDS) measurements showed that all x-ray peaks correspond to either Bi or Te (see Supporting Information S2).[12]

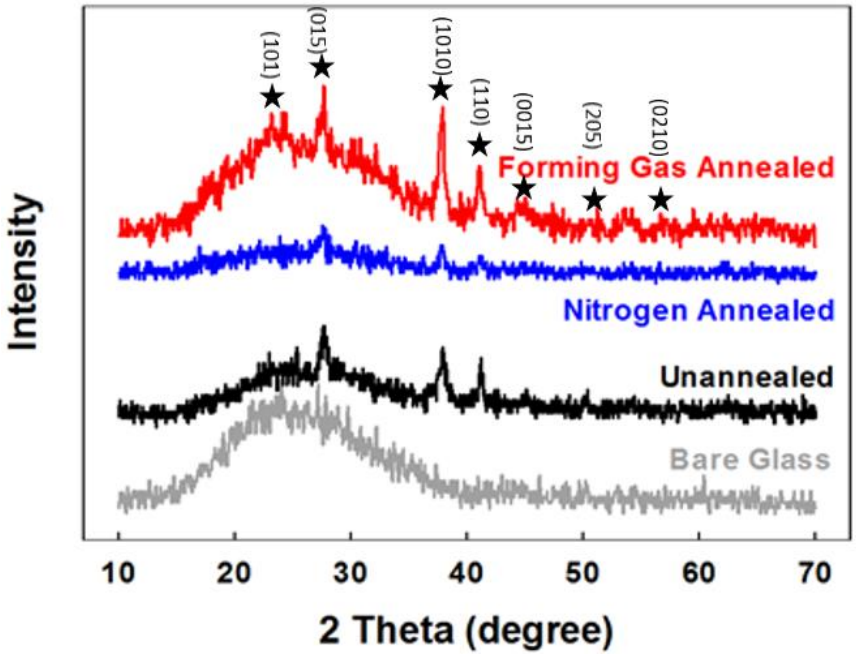

Figure 3. X-ray diffraction (XRD) measurements of bare glass substrate (grey), inkjet printed BTNWs that are un-annealed (black) and annealed in a nitrogen (blue) and forming gas (red)

ambient respectively. Sharp Bi_2Te_3 peaks (indexed) as well as the broad substrate peaks are portrayed while no impurity peaks are observed. The thickness of the printed BTNW networks correspond to 100 printing passes. As a reference, '*' symbols are shown to provide the position of the peaks and indices corresponding to a Bi_2Te_3 film.

Thermal annealing, in general, plays an important role on the network formation by providing input thermal excitation to the system and in rearranging the network geometry in an optimum manner. More importantly, a controlled annealing such as the ones used in the present work maintains oxidation free nano-materials processing, cleans the surfactants and surface of the nanowires, and introduces crystalline wire-wire nano-joints by forming active electronic conduction channels. Compared to annealing in a nitrogen ambient a forming gas annealing provides additional electronic passivation of active defects (such as dangling bonds) present on the network. Moreover, the pronounced microstructure changes observed in forming gas annealing could arise from high temperature annealing with exposure to high energy hydrogen radicals. Next, the electrical conductivity of the printed BTNWs was acquired for networks annealed in nitrogen and forming gas ambient with varying thicknesses (*i.e.*, 25 print layers ~ 0.4 μm thick, 50 print layers ~ 0.75 μm thick, 75 print layers ~ 1.1 μm thick, 100 print layers ~ 1.6 μm thick) (Figure 4a). The dependence of the room temperature electrical conductivity and thermal diffusivity of the distinctly annealed BTNW films on the thickness of the film is portrayed in Figure 4a and Figure 4c. The film with sparse NW density (corresponding to 25 printing passes) displayed an electrical conductivity of ~ 800 to 1200 S/m, a value that is roughly an order of magnitude smaller than recently reported metallic nanowire (*i.e.*, silver nanowire) networks that were inkjet printed with comparable thickness.[34] The lower electrical conductivity of the printed BTNWs, as compared to the metallic nanowires, is most likely due to the higher energy gaps of semiconductor materials as compared to the overlapping Fermi levels associated

with a conduction band of typical metallic materials. Also, the electrical conductivity of the BTNW network changes according to BTNW thickness or density as dictated by the number of printer passes used to create the networks (*i.e.*, 50, 75, and 100 printer passes). For example, the electrical conductivity initially increases from approximately 0.45 S/m $\times 10^3$ to 0.75 S/m $\times 10^3$ as the number of printer passes increases from 25 to 50 for the BTNWs annealed in forming gas, and then finally drops in electrical conductivity for printer pass thickness greater than 75 printer passes. The initial increase in electrical conductivity is most likely due to increased electrical pathways with increasing BTNW thickness. Finally, a saturation point is reached where the forming gas annealing process is no longer capable of penetrating the entire thickness of the film and un-annealed underlying BTNWs that contain numerous inter-trapped tube/tube connections that have not been passivated most likely increase the overall electrical resistance of the BTNW network. In contrast, for nitrogen annealed printed BTNWs the trend is different; the electrical conductivity of the nitrogen annealed BTNWs remains unchanged up to a thickness of 50 printer pass layers and then drops to nearly half of the conductivity with a film thickness of 25 printer pass layers. Thus, nitrogen annealing has minimal effect on the electrical conductivity of the BTNW films—a phenomenon that corroborates the lack of morphology changes in the BTNW nanowires and the slight deterioration of the crystallinity of the BTNWs upon nitrogen annealing as illustrated previously in Figure 2 and 3 respectively.

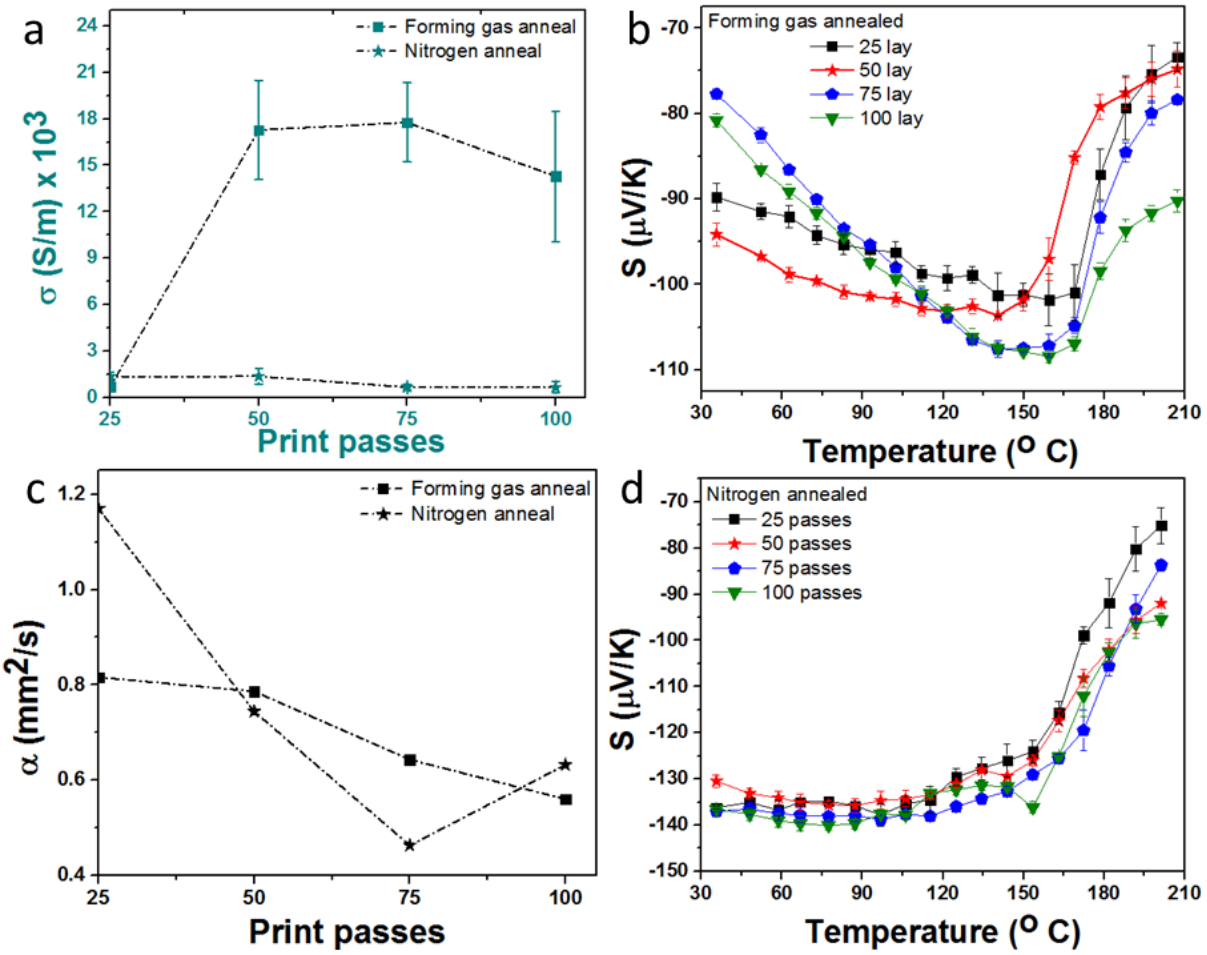

Figure 4. Room temperature electrical conductivity, room temperature thermal diffusivity and temperature dependent Seebeck coefficients of all eight printed films are shown; **(a)** and **(c)** show the electrical conductivity vs. thickness and the thermal diffusivity vs. thickness respectively of the printed BTNWs annealed in a forming gas and nitrogen gas ambient; **(b)** and **(d)** show the Seebeck coefficient of the printed BTNWs of varying thickness annealed in a forming gas and nitrogen gas ambient respectively measured at various temperatures (35 - 200°C by increments of 10°C). Various film thicknesses tested are 0.4 μm, 0.75 μm, 1.1 μm, and 1.6 μm which correspond to printing passes of 25, 50, 75 and 100 respectively.

Thermal transport was also evaluated to assess the thermoelectric properties of the printed BTNW networks. Thermal transport was monitored by measuring the thermal diffusivity (characteristic time a phonon takes for the temperature to attain a steady state) of the BTNW networks with a transient electro-thermal (TET) technique performed in a similar fashion to previous reports (see Supporting Information S4 for details).[35, 36] A square pulse direct current is typically fed through the sample to induce joule heating in the network and the variation of

voltage over the sample length is measured while the temperature evolves before reaching the steady state. This TET technique has been used to assess the thermal and electrical properties of wire/wire junctions in metallic NW networks,[37] however, no such study has been made in thermoelectric NW networks such as the printed BTNWs presented in this work. The temperature (T) change with time (t) is modeled following 1D heat transfer equation that involves the thermal diffusivity as below

$$\frac{\partial(\rho C_p T)}{\partial t} = \kappa \frac{\partial^2 T}{\partial x^2} + q_0 \qquad \text{(Eq. 1)}$$

Where, ρ is the density, κ is the thermal conductivity, C_p is the heat capacity of the sample and $\alpha = (\kappa/\rho C_p)$ is the intrinsic thermal diffusivity of the sample. q_0 is a constant relating to the electrical heating power per unit volume [35]. The theoretical solution to the above 1D thermal transport is given by [35]

$$T^* = \frac{96}{\pi^4} \sum_{m=1}^{\infty} \frac{1 - \exp(-(2m-1)^2 \pi^2 \alpha t / L^2)}{(2m-1)^4} \qquad \text{(Eq, 2)}$$

where α and L are the thermal diffusivity and length of sample, and t is time. Experimentally, the solution (T^*_{exp}) is simply obtained based on the voltages obtained in the sample as

$$T_{exp}{}^* = \frac{V_{wire} - V_0}{V_1 - V_0} \qquad \text{(Eq. 3)}$$

Where V_{wire} is the voltage evolution measured (in our case in an oscilloscope), V_1 is final voltage caused by joule heating (current induced) and V_0 is voltage before the pulse application. A fitting program developed was used to extract the thermal diffusivity data from theoretical and

experimental analysis. The thermal diffusivity was evaluated for BTNWs annealed in both forming and nitrogen gas environments with different thicknesses (25, 50, 75, and 100 printer passes respectively) (Figure 4a & 4c). All printed BTNW networks generally show a gradual decreasing trend in the thermal diffusivity with increasing film density/thickness. These measured thermal diffusivity values fall within a range of 0.56 mm^2/s - 0.8 mm^2/s for forming gas annealed samples and 0.45 mm^2/s - 1.17 mm^2/s for nitrogen annealed samples.

Next the Seebeck coefficient, a measure of the thermoelectric sensitivity, was measured to further assess the thermoelectric efficiency of the printed BTNWs (see details in Experimental & Supporting Information S3 and results in Figure 4b & 4d). The Seebeck coefficient values for the printed BTNWs are negative which is indicative of the dominant contribution of electron carriers that arise from Te-rich Bi_2Te_3 nanowires.[12] The magnitude of Seebeck coefficient between 75 μV/K and 140 μV/K at room temperature. The distinctly annealed BTNW films show different temperature dependent Seebeck coefficient trends. Printed BTNWs annealed with forming gas display an increasing (in negative direction) trend for Seebeck coefficient from RT to ~ 140 - 170°C, a constant trend between ~ 140 - 170°C, and a decreasing trend for temperatures above ~ 170°C. Films with nitrogen annealing, however, show constant and generally higher Seebeck coefficient values that sharply decrease after a temperature of approximately ~ 125°C. Higher Seebeck values for nitrogen annealed samples could be possible due to the higher carrier concentration. The increasing (in negative direction) Seebeck values from RT to ~ 140°C is indicative of degenerate semiconductor (semimetal) behavior. In the temperature regime between ~ 140 and 170°C, the excess hole contribution and electronic contribution to the transport remain balanced (with net negative and nearly constant Seebeck values) after which the contribution of hole substantially increases. The overall Seebeck values

still remain electron dominated at 400°C. Similar thermally induced hole-generation and hole-transport at temperatures beyond 125°C is also shown for films of all thicknesses considered in case of nitrogen annealed films. On the other hand, the relative stable value of the Seebeck coefficient in nitrogen annealed sample up to ~ 125°C indicates the negligible influence on electronic property of the network. Beyond 125°C a decrease in (electronic) Seebeck value is indicative of emergence of hole transport similar to the forming gas annealed case.

Finally, the room temperature power factor ($PF = \sigma S^2$ where σ and S are electrical conductivity and Seebeck coefficient) was calculated to better assess the overall thermoelectric capability of the printed BTNW films (Figure 5). Once the thickness of the BTNW films reached 50 print passes or higher the disparity in the PF value between the distinctly annealed samples is significant (note that for low density/thickness BTNW films the electrical conductivity plays a more significant role than the Seebeck coefficient and resultant PF values for the printed BTNWs are low for both annealing scenarios). Thus although the room temperature Seebeck coefficient for nitrogen annealed films are superior than those of the forming gas annealed ones, the overall product of electrical conductivity and the Seebeck coefficient, *i.e.*, the PF value, is higher. Subsequently, the resultant ZT value [$ZT = S^2\sigma T/k$ (where Z is the figure of merit, T is the absolute temperature, S is the Seebeck coefficient, and k is the total thermal conductivity)] of the forming gas annealed printed BTNWs would also be higher; the forming gas annealed printed BTNWs will have a higher heat-to-electricity conversion. The obtained PF of 163 $\mu W/m^{-1}K^{-2}$ is higher than the previous reported PF of inkjet-printed $Sb_{1.5}Bi_{0.5}Te_3$ powders (116 $\mu W/m^{-1}K^{-2}$)[8] and dispenser printed Bi_2Te_3 powder (158 $\mu W/m^{-1}K^{-2}$)[22]. Using $ZT = S^2\sigma T/k = (PF)T/(x\rho C_p\alpha)$ with the above PF and diffusivity values for 50 print passes obtained in this work, along with roughly 25% of fill factor (x) of the wires,

bulk Bi_2Te_3 density of 7.7 g/cm^3 (ρ), and bulk Bi_2Te_3 heat capacity (C_p) of 124.65 J/mol a room temperature figure of merit (or TE efficiency) of 0.26 and 0.05 were estimated for forming gas annealed and nitrogen annealed BTNW films respectively. In terms of the print parameters used in this work, a ~ 15 mm x 15 mm area could be efficiently printed with the TEG nanowires using our inkjet printer.

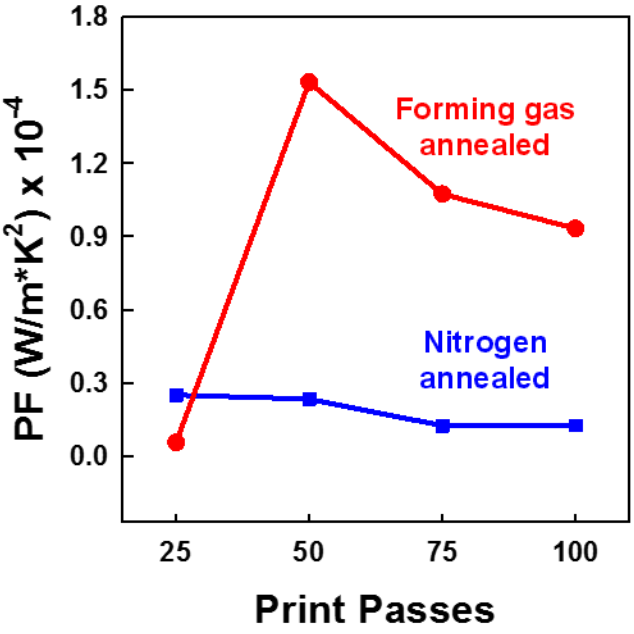

Figure 5. Power factor of the printed BTNWs samples of varying thickness (*i.e.*, 25, 50, 75 and 100 printer passes) annealed in a forming (red) and nitrogen (blue) gas ambient.

2.4 Conclusion

In summary, for the first time a single crystalline Bi_2Te_3 nanowire ink has been formulated and inkjet printed. Structural, microstructural, electrical, thermal, and thermoelectric characterizations of the printed patterns were made to demonstrate its applications. The printed BTNW networks display a Seebeck coefficient up to 140 µV K^{-1} which is on the same order of magnitude than BTNWs hot pressed into pellet form (~200 µV K^{-1}), while the amount of Bi_2Te_3 used in the printed BTNWs is ~ 1% to 3% of the material that is used in their bulk

counterparts.[12] This work demonstrates that inkjet printing of n-type telluride-based nanowires is possible and hence the subsequent fabrication of a printed thermoelectric generator (with both n-type and p-type elements/legs) should also be achievable. Other groups have developed techniques to inkjet print bismuth telluride powders, while nanowires that have number of advantages over the powders including electronic transport, have first been studied in this printed form. Our report shows for the first-time inkjet printing of Bi_2Te_3 nanowires with an achieved high power factor (163 $\mu W/m^{-1}K^{-2}$) and TE efficiency (ZT ~ 0.26) at room temperature. Thus, this work helps to pave the way for the scalable roll-to-roll manufacturing of thin film, printed thermoelectrics.

2.5 Experimental Section

Nanowire synthesis: TeO_2 powder (99.999%), potassium hydroxide, polyvinylpyrrolidone (PVP), ethylene glycol (EG), hydrazine hydrate, and $Bi(NO_3)_3.5H_2O$ were acquired from Sigma Aldrich. The printable BTNW ink was created by first mixing 0.2 gm of PVP, 0.6 gm of KOH, and 0.4788 gm of TeO_2 powder into a thermally insulated controlled 3-neck glass flask that is heated to 160°C and maintained at this temperature throughout the entire BTNW synthesis process. After an hour of heating, ~ 1 ml of hydrazine hydrate is injected into the solution to help reduce the TeO_2 and form tellurium nanowires. Next, a bismuth precursor solution is prepared by mixing 0.82 gm of $Bi(NO_3)_3.5H_2O$ into 5 ml of EG. This bismuth precursor solution is then added into the tellurium nanowire solution at 160°C and after approximately 1 hour the final BTNWs can be extracted and further processed for printing.

Ink formulation: To formulate the jettable ink, 5 ml of the liquid phase synthesized BTNWs are added to 10 ml of DI water. The mixture is then aliquoted and distributed into smaller Eppendorf tubes (1 mL of solution added to each tube) for subsequent centrifugation.

The BTNWs are centrifuged at 10,000 rpm for 5 mins, the resultant supernatant solution is then removed. The BTNW pellet is then redispersed in DI water (1 ml of DI added to each tube and then vortexed on low settings), centrifuged again, and the resultant supernatant removed again. This washing process is repeated for three times in order to remove ethylene glycol, KOH and hydrazine from the original BTNW stock solution. The sediment was collected and re-dispersed in DI water. Next, 2 hours of water bath sonication was performed to well disperse the Bi_2Te_3 NWs in DI water. The resultant ink exhibited high stability and could be stored at 4°C for 2 months without sedimentation.

Inkjet printing of Bi_2Te_3 thermoelectric nanowires (BTNWs): *The glass printing substrates were cleaned with acetone, isopropanol, and methanol respectively, and were then dried with nitrogen gas before use. To print the BTNWs onto the glass, 3 ml of the formulated ink was loaded into a printer cartridge that supplied a piezoelectric controlled printer head with 16 nozzles of a Fujifilm Dimatix Materials Printer system (Model DMP-2831). Printer patterns were CAD designed in Solidworks and then converted into an equivalent printable bitmap file that is compatible with the software capabilities of the Dimatix Materials Printer. The glass substrates were secured to a heated vacuum platen maintained at a temperature of 50°C during the heating process. Before printing, the voltage on each nozzle were modified (21-24 V) based on drop geometry visualized from the drop watcher while the number of printed layers (i.e., 25, 50, 75, 100 single print passes) were varied.*

Annealing of inkjet printed BTNWs: *The printed BTNW samples were left on the heated vacuum platen (temperature of 50°C) for an additional hour after printing to further remove/evaporate moisture. The printed BTNWs were subsequently annealed in a tubular furnace with two different recipes: recipe 1: annealing at 400℃ with forming gas flow (5%*

Hydrogen in Argon) for 2 hours, and recipe 2: annealing at 400℃ with nitrogen gas flow for 2 hours respectively. To avoid atmospheric oxidation of NWs surface, the samples were kept within a glove box after the annealing processes were completed.

Imaging and thickness measurements*: Field Emission Scanning Electron Microscopy (FESEM) images were measured using a FEI Quanta 250 in secondary electron mode using 10 kV accelerating voltage with the sample surface kept at ~ 10 mm of working distance from the field emitter source aperture. An Oxfords Instruments Aztec X-Max 80 detector system connected to FEI Quanta 250 was used to collect the EDX photons for elemental detection. The thickness of all samples was measured using a surface profilometer and hence the number of printer passes correlated to the following thickness measurements: 25 print layers ~ 0.4 μm thick, 50 print layers ~ 0.75 μm thick, 75 print layers ~ 1.1 μm thick, 100 print layers ~ 1.6 μm thick.*

X-ray diffraction (XRD) measurement: *The XRD measurements are performed using a powder diffractometer (Model Rigaku's Ultima IV) with CuKα radiation (λ ~ 1.5418 A°). BTNWs printed on a glass slides were scanned from 10° to 70° at a scan rate of 0.02° per second.*

Electrical conductivity measurements: *The electrical conductivity was measured using a four-probe resistivity measurement set up (Jandel multi height probe with RM 3000 test unit). The outer two probes were used to send current into the structure while the inner two probes were used to read the potential difference. The room temperature electrical conductivity of the printed nanowire films was calculated in conjunction with the average thickness information previously measured.*

Thermal diffusivity measurements: *Thermal diffusivity is measured using a transient electro-thermal technique reported earlier.*[35] *Briefly, sample is suspended in air and is held*

with silver paste between two copper electrodes. A direct electric current is passed through the sample to induce joule heating. The resulted voltage-time relationship is recorded by an oscilloscope. The data is then processed by pre-defined equations in MATLAB. It should also be noted that the BTNWs are printed on glass and therefore the thermal diffusivity results contain a contribution from the kapton (albeit small) in addition to the printed BTNWs. Also, the measurement results excludes any contribution originating from radiation (see Supporting Information S4 & S5).

Seebeck coefficient measurements: *Seebeck coefficient measurements of all the printed samples are performed under vacuum using a LSR - 3 Linseis - Seebeck coefficient and electric resistivity measurement unit. The printed pattern on glass substrate was first coated with silver paint at both the ends of the printed pattern in such a way that the silver contact spreads over the edges of the substrate. The sample was then vertically positioned between the two electrodes and a temperature gradient was applied across the sample as the electrodes serve as a heater and a heat sink (see the supporting information file for the schematic of the measurement set up and the temperature gradient). The potential difference generated in their vicinity (with maximum temperature fluctuations within couple hundred of milli kelvin and a voltage resolution of tens of nano volts) were measured.*

2.6 References

[1]L. A. Fisk, Science 2005, 309, 2016.

[2]S. J. Kim, J. H. We, B. J. Cho, Energy Environ. Sci. 2014, 7, 1959.

[3]M. Hyland, H. Hunter, J. Liu, E. Veety, D. Vashaee, Applied Energy 2016, 182, 518.

[4]G. J. Snyder, Electrochem. Soc. Interface 2008, 17, 54.

[5]A. Date, A. Date, C. Dixon, A. Akbarzadeh, Renewable Sustainable Energy Rev. 2014, 33, 371.

[6]D. M. Rowe, *CRC handbook of thermoelectrics*, CRC press, 1995.

[7]J. Lee, H. J. Kim, L. Chen, S. H. Choi, G. N. Mathur, V. K. Varadan, Proc. SPIE 8691, Nanosensors, Biosensors, and Info-Tech Sensors and Systems 2013, 86910R (16 April 2013); doi: 10.1117/12.2009765

[8]Z. Lu, M. Layani, X. Zhao, L. P. Tan, T. Sun, S. Fan, Q. Yan, S. Magdassi, H. H. Hng, Small 2014, 10, 3551.

[9]A. I. Hochbaum, R. Chen, R. D. Delgado, W. Liang, E. C. Garnett, M. Najarian, A. Majumdar, P. Yang, Nature 2008, 451, 163.

[10] L. Hicks, M. Dresselhaus, Phys. Rev. B 1993, 47, 16631.

[11] Y. Xia, P. Yang, Y. Sun, Y. Wu, B. Mayers, B. Gates, Y. Yin, F. Kim, H. Yan, Adv. Mater. 2003, 15, 353.

[12] G. Zhang, B. Kirk, L. A. Jauregui, H. Yang, X. Xu, Y. P. Chen, Y. Wu, Nano Lett. 2011, 12, 56.

[13] H. Yang, S. W. Finefrock, J. D. Albarracin Caballero, Y. Wu, J. Am. Chem. Soc. 2014, 136, 10242.

[14] S. W. Finefrock, H. Fang, H. Yang, H. Darsono, Y. Wu, Nanoscale 2014, 6, 7872.

[15] B. Hamdou, J. Gooth, A. Dorn, E. Pippel, K. Nielsch, Appl. Phys. Lett. 2013, 103, 193107.

[16] Z.-G. Chen, G. Han, L. Yang, L. Cheng, J. Zou, Progress in Natural Science: Materials International 2012, 22, 535.

[17] J. A. Lee, A. E. Aliev, J. S. Bykova, M. J. de Andrade, D. Kim, H. J. Sim, X. Lepró, A. A. Zakhidov, J. B. Lee, G. M. Spinks, Adv. Mater. 2016.

[18] J. H. We, S. J. Kim, G. S. Kim, B. J. Cho, J. Alloys Compd. 2013, 552, 107.

[19] Z. Cao, E. Koukharenko, M. Tudor, R. Torah, S. Beeby, J. Phys. Conf. Ser., 2013, 476.

[20] D. Madan, A. Chen, P. K. Wright, J. W. Evans, J. Appl. Phys. 2011, 109, 034904.

[21] J. Lee, H. J. Kim, L. Chen, S. H. Choi, G. N. Mathur, V. K. Varadan, "Development of thermoelectric inks for the fabrication of printable thermoelectric generators used in mobile wearable health monitoring systems", presented at *SPIE Smart Structures and Materials+ Nondestructive Evaluation and Health Monitoring*, 2013.

[22] A. Chen, D. Madan, P. Wright, J. Evans, J. Micromech. Microeng. 2011, 21, 104006.

[23] Y. Yang, Z.-H. Lin, T. Hou, F. Zhang, Z. L. Wang, Nano Res. 2012, 5, 888.

[24] L. Fonseca, J.-D. Santos, A. Roncaglia, D. Narducci, C. Calaza, M. Salleras, I. Donmez, A. Tarancon, A. Morata, G. Gadea, Semicond. Sci. Technol. 2016, 31, 084001.

[25] S. R. Das, Q. Nian, A. A. Cargill, J. A. Hondred, S. Ding, M. Saei, G. J. Cheng, J. C. Claussen, Nanoscale 2016, 8, 15870.

[26] P. Maisch, K. C. Tam, L. Lucera, H.-J. Egelhaaf, H. Scheiber, E. Maier, C. J. Brabec, Org. Electron. 2016, 38, 139.

[27] S. G. Hashmi, M. Ozkan, J. Halme, S. M. Zakeeruddin, J. Paltakari, M. Gratzel, P. D. Lund, Energy Environ. Sci. 2016, 9, 2453.

[28] K.-H. Choi, J. Yoo, C. K. Lee, S.-Y. Lee, Energy Environ. Sci. 2016, 9, 2812.

[29] M. Engel, J. P. Small, M. Steiner, M. Freitag, A. A. Green, M. C. Hersam, P. Avouris, ACS Nano 2008, 2, 2445.

[30] L. Hu, D. Hecht, G. Grüner, Nano Lett. 2004, 4, 2513.

[31] R. Chen, S. R. Das, C. Jeong, M. R. Khan, D. B. Janes, M. A. Alam, Adv. Funct. Mater. 2013, 23, 5150.

[32] P. Serre, M. Mongillo, P. Periwal, T. Baron, C. Ternon, Nanotechnology 2014, 26, 015201.

[33] D.-m. Sun, M. Y. Timmermans, Y. Tian, A. G. Nasibulin, E. I. Kauppinen, S. Kishimoto, T. Mizutani, Y. Ohno, Nat. Nanotechnol. 2011, 6, 156.

[34] D. J. Finn, M. Lotya, J. N. Coleman, ACS Appl. Mater. Interfaces 2015, 7, 9254.

[35] J. Guo, X. Wang, T. Wang, J. Appl. Phys. 2007, 101, 063537.

[36] H. Lin, S. Xu, X. Wang, N. Mei, Small 2013, 9, 2585.

[37] Z. Cheng, M. Han, P. Yuan, S. Xu, B. A. Cola, X. Wang, arXiv preprint arXiv:1603.06845 2016.

CHAPTER 3. FLEXIBLE THERMOELECTRIC GENERATORS WITH INKJET-PRINTED BISMUTH TELLURIDE NANOWIRES AND LIQUID METAL CONTACTS

This chapter is modified from a paper published in "Nanoscale, 2019, 11, 5222-5230"

Bolin Chen, Matthew Kruse, Biao Xu, Ravi Tutika, Wei Zheng, Michael D. Bartlett, Yue Wu and Jonathan C. Claussen*

Bolin Chen, Matthew Kruse, Prof. J. C. Claussen

Mechanical Engineering, Iowa State University, Ames IA 50011, USA

*Corresponding Author E-mail: jcclauss@iastate.edu

Biao Xu, Wei Zheng, Prof. Yue Wu

Chemical and Biological Engineering, Iowa State University, Ames IA 50011, USA

Ravi Tutika, Prof. Michael D. Bartlett

Materials Science and Engineering, Iowa State University, Ames IA 50011, USA

3.1 Abstract

Solution phase printing of nanomaterials is becoming increasingly important for the creation of scalable flexible electronics including those associated with biomedical and energy harvesting applications. However, the use of solution-phase printed thermoelectric energy generators (TEGs) has been minimally explored. Herein we report a highly flexible inkjet-printed TEG. Bismuth telluride (Bi_2Te_3) and bismuth antimony telluride ($Bi_{0.5}Sb_{1.5}Te_3$) nanowires (NWs) are inkjet printed onto polyimide to form n-type and p-type legs for the TEGs. A post-print thermal annealing process is used to increase the thermoelectric performance of the printed NWs while eutectic gallium-indium (EGaIn) liquid metal contacts electrically connect the TEG legs in series. Annealing conditions for the combination of p/n legs are examined to

maximize the thermoelectric efficiency of the TEG prototype. The maximum power factor was found to be 180 $\mu W\ m^{-1}K^{-2}$ and 110 $\mu W\ m^{-1}K^{-2}$ for the Bi_2Te_3 and $Bi_{0.5}Sb_{1.5}Te_3$ nanowires respectively. A maximum power for the fully printed TEG device measured127 nW at a 32.5 K temperature difference. The performance of the TEG device does not diminish even after multiple bending experiments (up to 50 times) around a tight radius of curvature (rod - dia. 11 mm). Hence this inkjet-printed flexible TEG is a step towards a fully functional wearable TEG device.

3.2 Introduction

The recent development of large-area, solution-phase printing techniques has enabled the fabrication of low-cost flexible electronics for various unique applications including disposable chemical/biological sensors,[1–4] biocompatible cellular scaffolds/conduits[5], radio-frequency identification (RFID)-enabled antennas[6], supercapacitors[7–10], optoelectronics[11–14], and organic light-emitting diodes[10,15]. The advancement of such low-cost printed electronics is beginning to converge on the development of flexible wireless sensor networks (WSNs) that can monitor stress, corrosion, vibrations, thermal fluctuations, electrical signals, and biochemical targets on curvilinear structures including on piping/exhaust systems[16,17], the human body[18,19], and smart unmanned vehicles[20]. However, these sensor networks are often limited due to the bulk and rigidity of battery components that are needed for power and data transmission. Hence, researchers are developing energy harvesters to acquire power from alternative, ambient energy sources including those from vibration, light, and thermal gradients found throughout the environment including on the body[21,22]. Thermal gradients are of particular interest due to the fact that thermal energy is generated from within the target of interest and consequently is generally more steady and reliable than other ambient energy sources that may vary depending

upon weather, location, or movement[23]. Thermal energy harvesting also shows promise for the continual power of WSN devices due to their simple design that does not use complex parts nor fluid/electrolyte additives that require maintenance and produce emissions or waste[24,25].

Typically, thermoelectric generators (TEGs) have been utilized in large scale applications where temperature gradients are high, such as space probes[26] and engine exhaust pipes[27]. These high temperature grade applications typically use metal oxide thermoelectric materials that are not efficient for use in low-grade heat sources (temperatures sources < 120ºC[28]; *e.g.*, body, home applications, and mobile devices) where temperature gradients are small.[29] Recently, researchers have developed thermoelectric materials (e.g., bismuth telluride, antimony telluride, and bismuth antimony telluride) that experience increased efficiencies with relatively high ZT values (the dimensionless thermoelectric figure of merit ZT is defined as $\sigma S^2 T/k$ where σ is electrical conductivity, S is Seebeck coefficient, T is the average temperature between the hot side and cold side, and k is thermal conductivity) with a range from 0.5 to 1.5 at low-grade temperatures[30–34]. In particular, bismuth telluride (BT)-based alloys have proven to be some of the most efficient thermoelectric materials at low temperatures. More specifically, n-type bismuth telluride (BT) and p-type bismuth antimony telluride (BST) exhibit high ZT values at temperature ranges between 300 and 500 K. Furthermore, the doping/alloying and/or nanostructuring of these materials have exhibited further improvements in device performance[35–37].

TEGs with bismuth telluride-based alloys are generally made with macro-sized pellets with sizes and thicknesses in the millimeter range. Traditional TEGs are fabricated by hot pressing p/n type thermoelectric alloys formed into pellets that are electrically connected in series by metal contacts and typically sandwiched between two ceramic plates[38]. The pellets are

bulky and rigid and subsequently not conducive for incorporation into flexible TEGs. Hence researchers have begun the process to develop solution-phase printing techniques including screen printing[17,39], dispenser printing[40–42], spray printing[43] , and inkjet printing[44–46] to create flexible TEGs that are amenable to low-cost and scalable manufacturing techniques. For example, Kar-Narayan and coworkers demonstrated that flexible organic-inorganic Bi_2Te_3/ Sb_2Te_3 nanocrystals printed within a poly(3,4-ethylenedioxythiophene) polystyrene sulfonate matrix could achieve a power factor of 30 μW $m^{-1}K^{-2}$ [47]. These solution-phase printing processes contain distinct advantages and disadvantages. Screen printing and dispenser printing are typically employed for thick, lower resolution films (line resolution and film thickness > 100 μM)[40]. Screen and spray printing requires the use of a prefabricated metal stencil to pattern surfaces and generates ink waste in the form of ink residue on the stencil/shadow mask and squeegee/doctor blade. However, inkjet printing is approximately 4-5 times faster than screen printing (depending upon the material, nozzle diameter, and patterning technique used) and has demonstrated line resolutions of approximately 50 μm,[48,49] and even 20 μm *via* recently developed inkjet maskless lithography patterning techniques.[2] Moreover, inkjet printing like aerosol printing does not require the use of a stencil or shadow mask.

Herein, we report the development of the first flexible TEG created by inkjet printing. A low-temperature, chemical batch synthesis is performed to create both n-type and p-type thermoelectric nanowires (NWs) comprised of bismuth telluride (Bi_2Te_3: BT) and bismuth antimony telluride ($Bi_{0.5}Sb_{1.5}Te_3$: BST) respectively. These thermoelectric NWs are formulated into a jettable ink and printed onto flexible polyimide substrates. The thermoelectric capability of the film is monitored for distinct film thicknesses, post-annealing temperatures and bending conditions. The printed TEG delivered a maximum power of 127 nW at a 32.5 K temperature

difference. High flexibility is also achieved by connecting individual TEG legs in series with eutectic gallium-indium (EGaIn) liquid metal interconnects. Hence, the inkjet-printed flexible TEG is a significant step towards fully functional wearable TEG devices.

3.3 Results and Discussion

3.3.1 Fabrication of Printed TEG

BST and BT nanowires (NWs) are synthesized following our previously reported low-temperature, solution-phase synthesis method.[35] Briefly, tellurium dioxide with surfactant polyvinylpyrrolidone is reduced into tellurium NWs within a mixture of potassium hydroxide, ethylene glycol, and hydrazine (reduction agent). Next, bismuth, and antimony precursors are added to form the BST and BT NWs respectively (Figure 1a).[35,33] Both NW mixtures are transformed into a printable mixture *via* dilution in deionized water (DI) water, centrifugation for solvent removal, and bath sonication to homogeneously suspend the NWs in liquid media (see Methods) (Figure 1b-c). Both the concentration the and viscosity of the BST and BT NW inks (2.5 mg/mL and 1.62 cP for BT NW inks and 2 mg/mL and 1.35 cP for the BST NW inks respectively) were tuned by manipulating the concentration of ink constituents to improve the printing quality. Consequently, printer clogging was generally prevented by lowering the concentration of these ink constituents while ink splatter was prevented by raising their concentration. The resultant BST and BT NW inks are inkjet printed with varying thickness on polyimide by controlling the number of passes of the nozzles during the inkjet printing process (see Methods). Hence, the printed nanowires are named BST25, BST50, and BST100 for the BST nanowires printed with 25, 50, 100 printer passes and BT50, BT100, and BT150 for the BT NWs printed with 50, 100, and 150 passes (Figure 1d-f). The average thickness of the BT50, BT100, BT150, BST25, BST50, and BST100 printed nanowires correspond to thicknesses of 0.57μm ± 0.10, 0.89μm ± 0.06,1.56μm ± 0.05, 0.37μm ± 0.04, 0.62μm ± 0.08, and 0.94μm ±

0.12 measured *via* SEM analysis (see Figure S1 in Supplemental Information, ± 1 std. deviation with n = 4). It should be noted here that these NW film thicknesses are chosen based on their thermoelectric performance (e.g., Seebeck coefficient, electrical conductivity) as well as their ability to maintain flexibility as noted in subsequent sections. The printed NWs are consequently annealed in a tube furnace under forming gas at various temperature and time (Figure 1g) to improve their thermoelectric properties and then connected in series by EGaIn liquid metal[50]. Finally, a silicone elastomer coating is applied to encapsulate and protect the final device from the environment (Figure 1h).

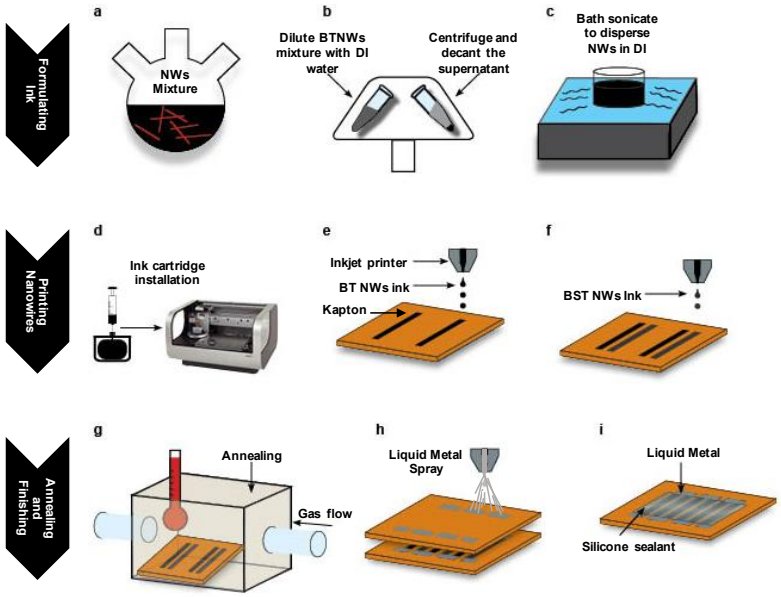

Figure 1. Fabrication schematic for the development of the inkjet printed TEG device. (**a-c**) Liquid phase synthesis of the BT and BST NWs and subsequent ink formulation for inkjet printing, (d-f) inkjet printing of the BT and BST NWs onto flexible polyimide film, (g) thermal annealing of printed NWs, and (**h-i**) spray printing of liquid metal contacts and doctor blade coating of silicone sealant.

3.3.2 Spectroscopic & Electrical Characterization of Printed Thermoelectric Nanowires

After inkjet printing (Fig. 1f), the thermoelectric NWs are thermally annealed or sintered (Fig. 1g) according to our previous protocols to improve their thermoelectric properties[46]. To improve the efficiency of device fabrication, an annealing temperature that maximized the

performance of both the BST and BT nanowires was explored. The annealing temperature of 400 °C induced within a forming gas environment (~ 2 hrs.) was first analyzed according to our previous results (see Methods)[46]. After annealing at these conditions, the printed BST50 form small and discrete crystalline NWs (Figure 2a). This process leads to large electrical resistance of the sample, most likely due to the lack of nanowire-to-nanowire sintering. However, at a higher annealing temperature (450 °C) and a shorter annealing time (10 mins) the printed BST50 nanowires morphology changed from discrete nanowires to agglomerated microdisks; the nanowires become sintered at these higher annealing temperatures (Fig. 2b). It should be noted that the annealing time was reduced from 2 hours to 10 minutes during annealing at 450 °C as the longer annealing time began to crack the printed BST50 nanowire film, disintegrate the polyimide substrate underlayer, and consequently render the sample electrically non-conductive (Figure S2 & S3). Similarly, BT50 printed nanowires become sintered at the elevated annealing conditions (*viz*., 450°C for 10 minutes) (Fig. 2c & 2d) with a noticeable lower change in morphology which is most likely due to the absence of the low melting point element antimony that is present in the BST NWs. Moreover, the electrical conductivity (measured at room temperature, see Methods) for the printed BST NWs annealed at these conditions was ~29900 S m^{-1} as compared to ~0 S m^{-1} with annealing at 450 °C for 2 hours (due to severe sample degradation), and ~617 S m^{-1} after annealing at 400 °C for 2 hours (see Methods). Similarly, the electrical conductivity (measured at room temperature) for printed BT NWs annealed at these conditions was 5649 S m^{-1} as compared to 63 S m^{-1} after annealing at 450 °C for 2 hours and 1204 S m^{-1} after annealing at 400 °C for 2 hours. It should be noted that these electrical conductivities are higher than recently reported $Bi_{1.8}Te_{3.2}$ and Sb_2Te_3 thick films comprised of printed powders [20]. Such a high electrical conductivity is most likely due to percolative nature of

the of the printed and thermally annealed nanowire network (~ 8 nm diameter nanowires) that may help maintain high electrical conductivities while suppressing phonon assisted thermal conductivity which would effectively increase the ZT values of the printed films[51]. In summary, the forming gas annealing at 450 °C for 10 mins significantly improved the electronic transport through the printed thermoelectric nanowires the most and hence was used in the final printed TEG prototype developed herein.

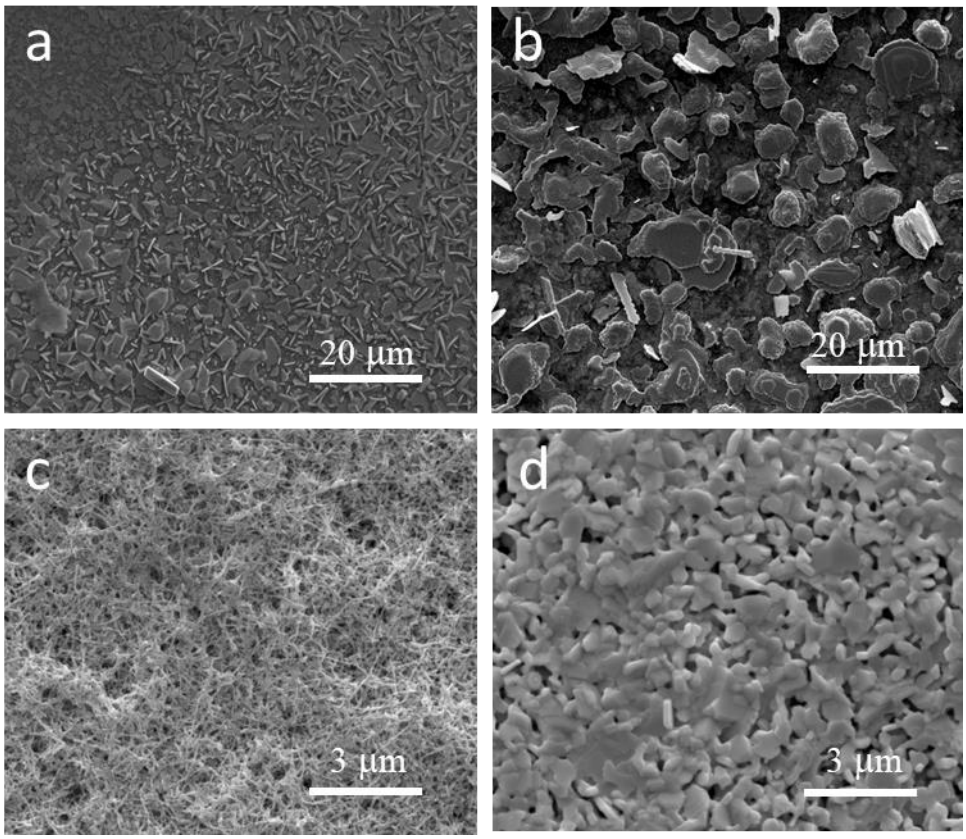

Figure 2. Scanning electron microscopy (SEM) micrographs displaying morphology changes of the printed BST50 and BT50 nanowires after thermal annealing. Printed BST50 NWs annealed at (**a**) 400°C for 2 hours and (**b**) 450 °C for 10 mins. Printed BT50 NWs annealed at (**c**) 400 °C for 2 hours and (**d**) 450 °C for 10 mins.

Next, X-ray diffraction (XRD) was used to verify the crystalline structure of the printed BST50 and BT50 NWs before and after annealing. Distinct peak positions for $Bi_{0.5}Sb_{1.5}Te_3$ (JCPDS-#49-1713) and Bi_2Te_3 (JCPDS-#15-863) are observed for the printed BST50 and BT50

NW samples respectively (Figure 3a & 3b). These XRD peaks become much more pronounced and sharp after the annealing process without an observable shift in their position. This suggests that annealing both the BST50 and BT50 printed NWs at 450 °C for 10 minutes improves the crystalline nature of the NWs without changing their phase or composition. Hence, these annealing conditions are conducted on all subsequent samples explored herein.

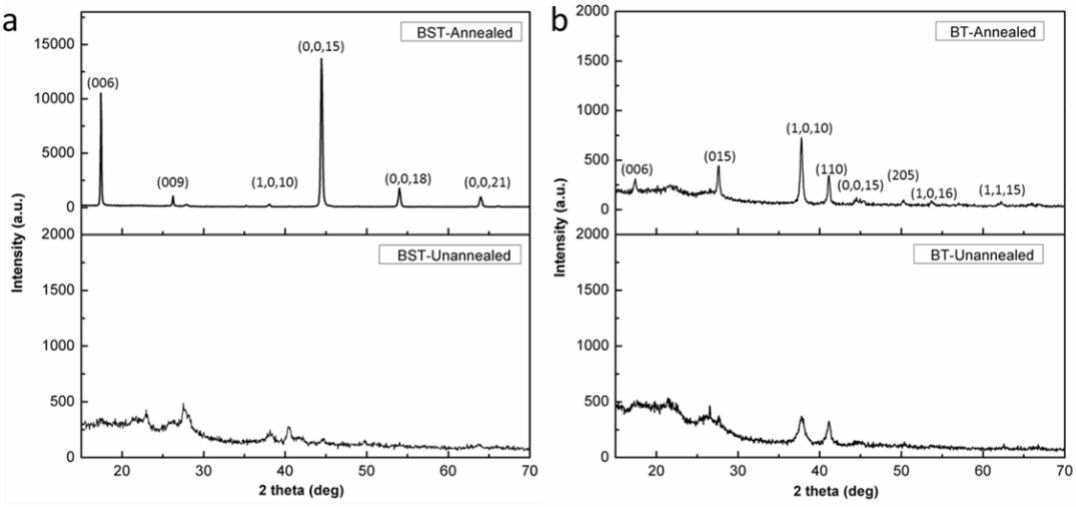

Figure 3. XRD diffraction patterns obtained from the printed (a) BST and (b) BT NWs. XRD patterns after annealing (top) and before annealing (bottom) at 450 °C for 10 mins.

3.3.3 Thermoelectric Characterization of Printed Thermoelectric Nanowires

The in-plane Seebeck coefficient (*S*), electrical conductivity (σ) and calculated power factor (*P.F.*) of the printed and thermally annealed BST25, BST50, and BST100 samples were acquired over a low-grade temperature range of 300 – 400 K. (Figure 4). First, the *S*, σ, and *P.F.* of all the printed BST NW samples were analyzed and plotted (Figure 4a-c). All BST samples display positive S values that are indicative of p-type behavior while the slight increase of S at higher temperature can be attributed to the thermal excitation of electrons[52]. The high S value for BST25 is possibly due to the low carrier concentration when the film is too thin (not continuous). BST25 has an electrical conductivity of approximately 400 S m^{-1}, which is considerably lower

than values recorded for the BST50 and BST100 printed NWs (Figure 4b). This low electrical conductivity of BST25 is most likely due to the poor film formation at such a low film thickness. However, the electrical conductivity of the thick BST100 printed NWs is consistently lower than the BST50 films as well. In the case, the thicker BST100 most likely experienced insufficient annealing (forming gas and heat did not sufficiently penetrate the sample) which lead to lower electrical conductivity. Consequently, the calculated power factor ($P.F. = \sigma * S^2$) for the BST50 printed NWs was higher than the BST50 and BST100 printed NWs (Figure 4c). The printed BST50 NWs displayed the highest *P.F.*, ~$1.8*10^{-4}$ W $m^{-1}K^{-2}$ at 400 K. Next, the *S*, σ, and *P.F.* of all the printed BT NW samples were also plotted (Figure 4d-f). The negative S values of BT samples are indicative of n-type behavior, and the values increase with the increase of measurement temperature. However, the printed BT50 and BT150 NWs display lower S values than printed BT100 NWs. This deviation could be attributed to the over-annealing of film with less materials on BT50 films and insufficient annealing of BT150 films, which would consequently decrease the electron mobility. In this case the BT100 printed films displayed a slightly higher electrical conductivity than the BT150 films and much higher electrical conductivity then the BST25 films. Again the thinnest film was most likely too thin for sufficient electrical transport. However, the annealing process sufficiently penetrated both the BST 100 and 150 printed films and their associated electrical conductivity improved with increasing temperature. These results are most likely due to the increase in grain size of the printed BST that occurred with increasing temperature which has shown to occur according to previous reports.[28] Consequently, the printed BT100 NW films displayed the highest *P.F.* value of $1.1 * 10^{-4}$ W $m^{-1}K^{-2}$ at 400 K. Moreover it is also likely that the high *P.F.* values for both the BST50 and BT100 samples are due in part to the reduction of wire-wire contact resistance

that occurs at elevated annealing temperatures where the superficial polyvinlpyrrolidone (PVP), present on the nanowires from the synthesis process, starts to decompose while the nanowires start to fuse together[53]. Moreover, the performance of the printed films exhibited low thermal conductivity due to the ability of the nanowire network films to increase phonon scattering[51]. On that note, the in-plane thermal conductivities of the prepared BT NWs and BST NWs were 1.19 W $m^{-1}K^{-1}$ and 0.55 W $m^{-1}K^{-1}$ respectively, as reported in our previous work[33,35]. Such thermal conductivities were hence used to estimate ZT values of 0.04 for the BT100 printed thin film and 0.13 for BST50 printed thin films annealed at 400 K.

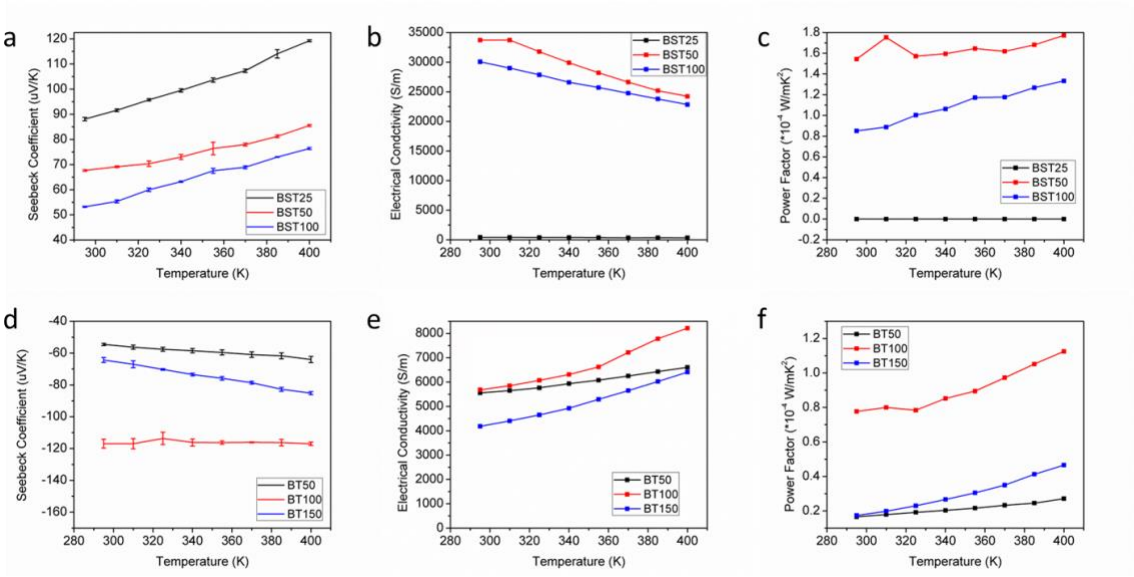

Figure 4. Temperature dependent thermoelectric property measurements: (a) Seebeck coefficient (*S*) (b) Electrical conductivity (σ) and (c) Power factor (*P.F.*) for the printed BST25, BST50, and BST100 NW films. (d) *S* (e) σ and (f) *P.F* for the printed BT50, BT100, and BT150 NW films. All measurements are acquired across a low grade temperature range of 300 to 400 K with increments of 50 K. Note, all graphs contain error bars (1 σ) which are acquired from three distinct samples (n = 3). Error bars are smaller than the symbol size for the electrical conductivity and power factor graphs.

3.3.4 TEG flexibility experiments

Finally, a fully functional flexible TEG prototype containing five pairs of legs was developed to test the ability of such a device to harvest energy from low-grade thermal gradients

(Figure 5 & Figure 1). It should be noted that the TEG prototypes fabricated with EGaIn contacts that electrically connect the p and n-type TEG legs, displayed better flexibility as compared to prototypes integrated silver paste electrical contacts (Figure S4). Consequently, all following experiments are carried out with prototypes fabricated with EGaIn electrical contacts. The performance of the TEG prototype was monitored by attaching the device to the curved surface of a plastic cup. A 0.1 mV baseline output voltage was measured when the water level was below the sample (no temperature difference across the sample). Next, DI water at 30 °C was then poured into the cup until the water level was even with the bottom height of the TEG EGaIn contacts (Figure 5b). In this scenario, the measured voltage increases to 9.8 mV due to the temperature difference between the water and the air (21 °C). The output power (P) of this TEG prototype was next calculated by using the equation $P = EI - I^2R_{in} = E^2R/(R + R_{in})^2$ where E is the open circuit voltage, I is the output current, R_{in} is the resistance of TEG and R is the load resistance. The TEG generates 14.1 nW with 10.5 mV at a 7 K temperature difference between the cold water and warmer ambient air (Figure 5f). This temperature difference is similar to the difference between the active human body temperature and ambient temperature.[54] A 127 nW maximum power is generated at a 32.5 K temperature difference with five pairs of p-n legs when the load resistance matches the TEG resistance as shown in Figure 5f. This power output is currently the highest reported value for thin film (thickness < 5 μm) thermoelectric generators (TEGs).[44,55]

Next, the flexibility and durability of the TEG prototype was analyzed. The TEG sample was rolled up around a rod with a radius of 11 mm (Figure 5c) in a cyclic fashion. A negligible change in resistance was measured as 4 kΩ for the printed TEG tightly wound around the rod and 3.9 kΩ for the unwound, flat TEG (Figure 5d insert). The durability of the sample was

monitored by measuring the resistance of the prototype after multiple bending/rolling cycles (1, 10, 20, 30, 40, 50; see Figure 5d). Once again, no significant change in resistance was found after these cyclic bending tests; the printed TEG prototypes demonstrate high flexibility and durability—attributes that generally cannot be achieved by TEGs fabricated with pellets or screen-printed thick films. Next, the open circuit voltage of the device was acquired at various temperature differences and plotted (Figure 5f). This measurement was performed by initially suspending the sample between a hot plate and a cold plate. A maximum voltage of 46 mV was created by a temperature difference of 32.5 K between the hot and cold plate. Three measurement trails were performed on the same sample and consequently one pair of the p-n TEG legs displayed a voltage of 160 uV K^{-1} with R=0.998, which is consistent with the *S* measured on the BST50 and BT100 printed films at the corresponding temperature (Figure 4a & c). Hence a similarly fabricated TEG device fabricated with 360 pairs of legs should theoretically (neglecting increased resistances with longer TEGs) generate 1.8 V and power a red light emitting diode at a temperature difference of 30 K.

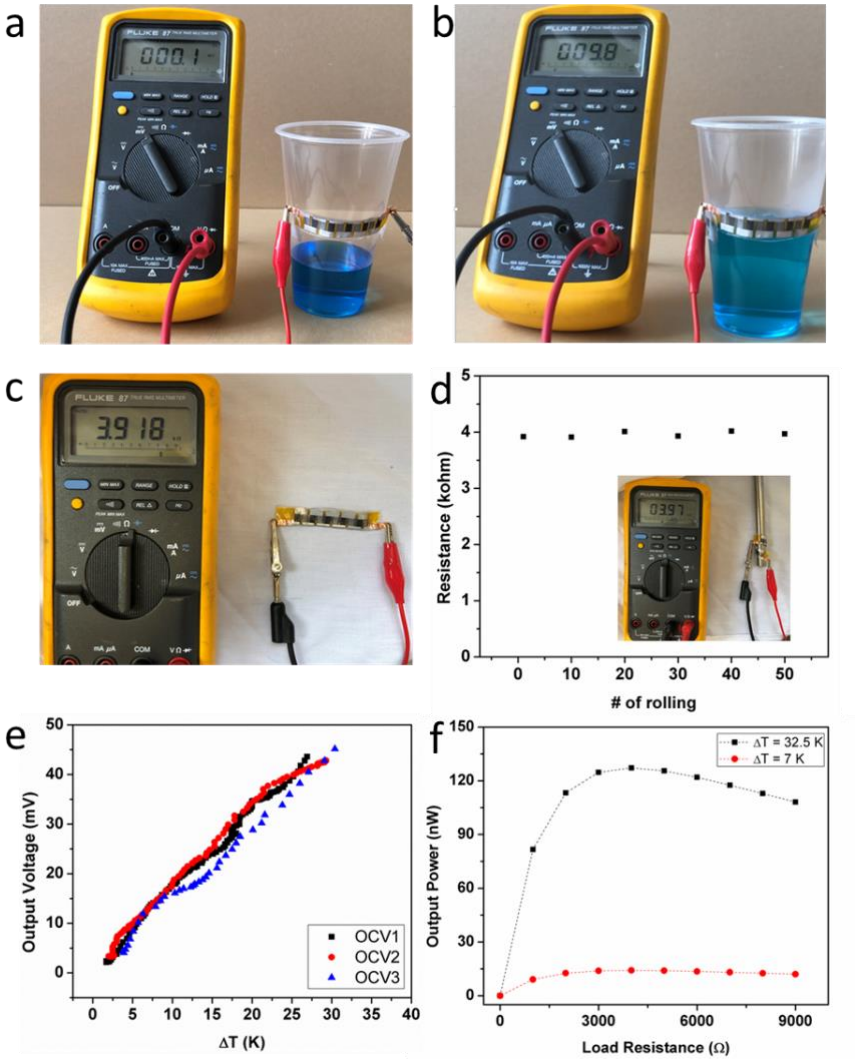

Figure 5. (a) An optical image of an inkjet-printed TEG prototype wrapped around a plastic cup while open circuit voltage is measured with a voltammeter. (b) The open circuit voltage reading after adding 40 °C water to the level of the bottom TEG EGaIn electrical contact. (c) The resistance of the printed TEG when unrolled in a flat position and (d) the resistance after tightly wrapping around a metal rod (dia. 11 mm) for 1, 10, 30, 40, 50 times of rolling. Inset picture portraying TEG tightly wrapped around the rod. (e) Three repetitions of open circuit voltage measurements acquired over varying temperatures of a printed TEGs containing 5 pairs of p-n legs. (f) The output power of the printed TEG as a function of load resistance.

3.4 Conclusion

In this work, a flexible thin-film TEG device is created with inkjet printed BST and BT NWs. Liquid metal contacts significantly increase the overall flexibility of the printed TEGs as

compared to traditional silver paste contacts. These developed fabrication protocols enable the scalable fabrication of thin film TEGs on flexible substrates and consequently helps pave the way for thermal energy harvesting from low temperature gradients and curved objects (*e.g.*, human body). A high power factor for the device (1.8 *10^{-4} W $m^{-1}K^{-2}$), relative to other thin-films, is achieved for the printed TEG prototype. The TEG prototype developed herein with five pairs of p-n legs delivered a 45 mV voltage while a temperature difference of 32.5 °C was maintained between the hot and cold ends. The power output of 127 nW is the highest reported value for an all-printed, thin film thermoelectric generator. Moreover, in general, inkjet printing is an additive manufacturing method that is a versatile and cost-effective approach to deposit 2D or 1D nanomaterials that does not require cleanroom technology or masks/stencils that are typically associated with e-beam evaporation, sputtering, or screen-printing. Hence, the annealing techniques and liquid metal contact deposition methods developed herein could be useful for not only thermoelectric energy harvesters[56] but also for other wearable energy harvesters such as solar[57,58], piezoelectric, and triboelectric devices[59–61] as well as medical-focused flexible biosensors[2,62–64] or nerve regrowth conduits[5] that require electrical contact even during cyclic flexing and/or during fitting with curvilinear forms.

3.5 Methods

3.5.1 Thermoelectric nanowire ink formulation

Distinct recipes were created for the development of BST and BT inks so that they were both amenable to inkjet printing. Both BST and BT ink were diluted with DI water and centrifuged to create a homogeneous ink suitable for inkjet printing. Briefly, the synthesized BST nanowire solution was diluted with DI water (3:1 ratio or 0.75 ml to 1.25mL) and centrifuged at 13,300 rpm for 10 minutes. The NWs were rinsed by removing the supernatant via pipetting and subsequently mixing the remaining wires in fresh DI water (1.25 mL) via

vortex mixing. A second centrifugation step (10,000 rpm for 5 mins) was performed and the consequent supernatant was removed. These removed nanowires were then remixed with fresh DI water (1.25 mL), and the resultant solution bath sonicated for 30 minutes to create a homogeneous jettable ink. The synthesized BT nanowire solution was formulated in a similar fashion with the following variations. BT ink was first diluted with DI water in the ratio of 1:1, and centrifuged at 12, 000 rpm for 10 minutes, followed by a second centrifugation at 10,000 rpm for 5 mins. The viscosity of the inks were measured using a Pheometer uVisc micropipette viscometer at 25 °C.

3.5.2 Inkjet printing of thermoelectric nanowires

A Diamtix 2381 inkjet printer was used to print the thermoelectric nanowires according to our previous protocols[46]. Briefly, inkjet printer cartridges (10 pL cartridges with 1.5 mL ink space volume) were filled with BST or BT NW ink and used to print the p-type and n-type nanowires respectively. The BST and BT nanowires were printed with varied printer passes 25 to 150) to examine the effect of film thickness on the thermoelectric performance. The temperature of the printer platen that holds the substrates during printing was set to 45°C. All NWs were printed directly onto flexible polyimide (Katpon®, McMaster-Carr) which a partially wettable substrate with a static water contact angle of ~ 63° (see Figure S5). This contact angle measurement was acquired by using a Goniometer where a droplet of 1.5µL water was dispensed onto the polyimide substrate through an integrated syringe pump. Captured images were analyzed with the assistance of ImageJ software.

3.5.3 Post-print nanowire annealing and liquid metal contact printing

Thermal annealing of the printed BST and BT nanowires were conducted simultaneously in a MTI single-zone furnace within a 2 inch diameter quartz tube. A steady stream of forming

gas (flow rate 50 mL min^{-1}, at atmosphere pressure) was used to fill the tube while the annealing temperature and time were varied between 400 °C and 450 °C and 10 mins and 2 hours respectively. After thermally annealing, EGaIn was used to electrically connect the printed NWs and form the TEG device. An EGaIn alloy was first prepared by mixing gallium and indium (Solution Materials, LLC) at a 3:1 ratio by mass and then heating the mixture at 200 °C overnight on a hot-plate to homogenize the alloy. To print the alloy, the BST and BT NWs already printed on flexible polyimide were masked with a laser-patterned tape and the EGaIn was coated onto unmasked polyimide to selectively deposit the EGaIn interconnects *via* a nitrogen-assisted spray coating procedure. After spray coating, the mask was removed and the printed EGaIn traces at the ends were connected to copper tape to facilitate electrical measurements. Finally, a thin layer of Pt-catalyzed silicone elastomer (Ecoflex 00-30, Smooth-On Inc.) was applied *via* doctor blade coating using a ZUA 2000 Universal applicator (Zehntner Testing Instruments) to encapsulate the device and protect the NWs from further oxidation.

3.5.4 Printed thermoelectric generator characterization

The complete thermoelectric generator (TEG) was characterized via electrical and thermoelectric measurements. In-plane electrical conductivity was measured by H5000 probe station with a temperature controller K2000, varying temperature from 295-400 K. Each sample was cut into 1 cm^2 square specimen for electrical measurements. The chamber held in vacuum (< 10 mTorr) during measurements. The in-plane Seebeck coefficient was measured by MMR SB1000 with a temperature controller K2000, varying temperature from 295-400 K. Seebeck measurement samples are cut into 1 mm by 6 mm strips and connected to sample holders with silver paste from Agar Scientific. A constantan wire was used as an internal reference. Open circuit potential and power output were measured with a Gamry reference 3000 electrochemical station by heating one side of the printed TEG *via* a hotplate over a temperature range of 45 to 80

°C, while the other side was placed on a cold plate (~23°C). The temperatures are recorded by thermometer with a computer-aid recorder.

3.5.5 Imaging and thickness measurements of the printed thermoelectric nanowires

SEM micrographs were acquired from a FEI Quanta-250 SEM in secondary electron mode using a 10 kV accelerating voltage. The working distance between the samples and the field emitter source aperture was kept at approximately 10 mm. XRD patterns were acquired from a powder diffractometer (Model Siemens D500 x-ray diffractometer) with CuK α radiation. All samples were scanned from 15º to 70º with a scan rate of 2 º min^{-1}.

3.6 References

1 Q. He, S. R. Das, N. T. Garland, D. Jing, J. A. Hondred, A. A. Cargill, S. Ding, C. Karunakaran and J. C. Claussen, *ACS Appl. Mater. Interfaces*, 2017, **9**, 12719–12727.

2 J. A. Hondred, L. R. Stromberg, C. L. Mosher and J. C. Claussen, *ACS Nano*, 2017, **11**, 9836–9845.

3 M. Medina-Sánchez, C. Martínez-Domingo, E. Ramon and A. Merkoçi, *Adv. Funct. Mater.*, 2014, **24**, 6291–6302.

4 M. V Kulkarni, S. K. Apte, S. D. Naik, J. D. Ambekar and B. B. Kale, *Sensors Actuators B Chem.*, 2013, **178**, 140–143.

5 S. R. Das, M. Uz, S. Ding, M. T. Lentner, J. A. Hondred, A. A. Cargill, D. S. Sakaguchi, S. Mallapragada and J. C. Claussen, *Adv. Healthc. Mater.*, 2017, **6**, 1–8.

6 V. Lakafosis, A. Rida, R. Vyas, L. Yang, S. Nikolaou and M. M. Tentzeris, *Proc. IEEE*, 2010, **98**, 1601–1609.

7 Z. Tehrani, D. J. Thomas, T. Korochkina, C. O. Phillips, D. Lupo, S. Lehtimäki, J. O'Mahony and D. T. Gethin, *Energy*, 2017, **118**, 1313–1321.

8 B. Chen, Y. Jiang, X. Tang, Y. Pan and S. Hu, *ACS Appl. Mater. Interfaces*, 2017, **9**, 28433–28440.

9 Y.-Z. Zhang, Y. Wang, T. Cheng, W.-Y. Lai, H. Pang and W. Huang, *Chem. Soc. Rev.*, 2015, **44**, 5181–5199.

10 T. Cheng, Y.-Z. Zhang, J.-P. Yi, L. Yang, J.-D. Zhang, W.-Y. Lai and W. Huang, *J. Mater. Chem. A*, 2016, **4**, 13754–13763.

11 S.-G. Li, K.-J. Jiang, M.-J. Su, X.-P. Cui, J.-H. Huang, Q.-Q. Zhang, X.-Q. Zhou, L.-M. Yang and Y.-L. Song, *J. Mater. Chem. A*, 2015, **3**, 9092–9097.

12 F. C. Krebs, *Sol. Energy Mater. Sol. Cells*, 2009, **93**, 394–412.

13 D. Li, W.-Y. Lai, Y.-Z. Zhang and W. Huang, *Adv. Mater.*, 2018, **30**, 1704738.

14 T. Cheng, Y. Zhang, W.-Y. Lai and W. Huang, *Adv. Mater.*, 2015, **27**, 3349–3376.

15 L. Zhou, M. Yu, X. Chen, S. Nie, W.-Y. Lai, W. Su, Z. Cui and W. Huang, *Adv. Funct. Mater.*, 2018, **28**, 1705955.

16 B. Orr, A. Akbarzadeh, M. Mochizuki and R. Singh, *Appl. Therm. Eng.*, 2016, **101**, 490–495.

17 B. Iezzi, K. Ankireddy, J. Twiddy, M. D. Losego and J. S. Jur, *Appl. Energy*, 2017, **208**, 758–765.

18 G. Fortino, R. Giannantonio, R. Gravina, P. Kuryloski and R. Jafari, *IEEE Trans. Human-Machine Syst.*, 2013, **43**, 115–133.

19 M. D. Bartlett, E. J. Markvicka and C. Majidi, *Adv. Funct. Mater.*, 2016, **26**, 8496–8504.

20 Z. Cao, E. Koukharenko, M. J. Tudor, R. N. Torah and S. P. Beeby, *Sensors Actuators, A Phys.*, 2016, **238**, 196–206.

21 C. Alippi and C. Galperti, *IEEE Trans. Circuits Syst. I Regul. Pap.*, 2008, **55**, 1742–1750.

22 S. J. Kim, J. H. We and B. J. Cho, *Energy Environ. Sci.*, 2014, **7**, 1959.

23 M. Hamid Elsheikh, D. A. Shnawah, M. F. M. Sabri, S. B. M. Said, M. Haji Hassan, M. B. Ali Bashir and M. Mohamad, *Renew. Sustain. Energy Rev.*, 2014, **30**, 337–355.

24 G. G. Yadav, J. A. Susoreny, G. Zhang, H. Yang and Y. Wu, *Nanoscale*, 2011, **3**, 3555.

25 W. He, G. Zhang, X. Zhang, J. Ji, G. Li and X. Zhao, *Appl. Energy*, 2015, **143**, 1–25.

26 L. A. Fisk, *Science (80-.).*, 2005, **309**, 2016–2017.

27 J. Yang and F. R. Stabler, *J. Electron. Mater.*, 2009, **38**, 1245–1251.

28 M. Reznikov and P. Wilkinson, *IEEE Trans. Ind. Appl.*, 2014, **50**, 4233–4238.

29 X. Xu, A. J. Karis, M. J. Buller and W. R. Santee, *Eur. J. Appl. Physiol.*, 2013, **113**, 2381–2389.

30 Y. Zheng, Q. Zhang, X. Su, H. Xie, S. Shu, T. Chen, G. Tan, Y. Yan, X. Tang, C. Uher and G. J. Snyder, *Adv. Energy Mater.*, 2015, **5**, 1–11.

31 L. P. Hu, T. J. Zhu, Y. G. Wang, H. H. Xie, Z. J. Xu and X. B. Zhao, *NPG Asia Mater.*, 2014, **6**, e88-8.

32 G. Zheng, X. Su, X. Li, T. Liang, H. Xie, X. She, Y. Yan, C. Uher, M. G. Kanatzidis and X. Tang, *Adv. Energy Mater.*, 2016, **6**, 1–12.

33 G. Zhang, B. Kirk, L. A. Jauregui, H. Yang, X. Xu, Y. P. Chen and Y. Wu, *Nano Lett.*, 2012, **12**, 56–60.

34 W. Xie, X. Tang, Y. Yan, Q. Zhang and T. M. Tritt, *Appl. Phys. Lett.*, 2009, **94**, 1–4.

35 B. Xu, M. T. Agne, T. Feng, T. C. Chasapis, X. Ruan, Y. Zhou, H. Zheng, J.-H. Bahk, M. G. Kanatzidis, G. J. Snyder and Y. Wu, *Adv. Mater.*, 2017, **29**, 1605140.

36 D. Kraemer, Q. Jie, K. McEnaney, F. Cao, W. Liu, L. A. Weinstein, J. Loomis, Z. Ren and G. Chen, *Nat. Energy*, 2016, **1**, 16153.

37 C.-L. Hsin, M. Wingert, C.-W. Huang, H. Guo, T.-J. Shih, J. Suh, K. Wang, J. Wu, W.-W. Wu and R. Chen, *Nanoscale*, 2013, **5**, 4669.

38 J. R. Lim, J. F. Whitacre, J. P. Fleurial, C. K. Huang, M. A. Ryan and N. V. Myung, *Adv. Mater.*, 2005, **17**, 1488–1492.

39 S. H. Park, S. Jo, B. Kwon, F. Kim, H. W. Ban, J. E. Lee, D. H. Gu, S. H. Lee, Y. Hwang, J.-S. Kim, D.-B. Hyun, S. Lee, K. J. Choi, W. Jo and J. S. Son, *Nat. Commun.*, 2016, **7**, 13403.

40 A. Chen, D. Madan, P. K. Wright and J. W. Evans, *J. Micromechanics Microengineering*, 2011, **21**, 104006.

41 M. K. Kim, M. S. Kim, S. E. Jo and Y. J. Kim, *Electron. Lett.*, 2012, **48**, 1015–1017.

42 D. Madan, Z. Wang, A. Chen, R. Winslow, P. K. Wright and J. W. Evans, *Appl. Phys. Lett.*, 2014, **104**, 013902.

43 E. J. Bae, Y. H. Kang, K.-S. Jang, C. Lee and S. Y. Cho, *Nanoscale*, 2016, **8**, 10885–10890.

44 A. Besganz, V. Zöllmer, R. Kun, E. Pál, L. Walder and M. Busse, *Procedia Technol.*, 2014, **15**, 99–106.

45 Z. Lu, M. Layani, X. Zhao, L. P. Tan, T. Sun, S. Fan, Q. Yan, S. Magdassi and H. H. Hng, *Small*, 2014, **10**, 3551–3554.

46 B. Chen, S. R. Das, W. Zheng, B. Zhu, B. Xu, S. Hong, C. Sun, X. Wang, Y. Wu and J. C. Claussen, *Adv. Electron. Mater.*, 2017, **3**, 1600524.

47 C. Ou, A. L. Sangle, A. Datta, Q. Jing, T. Busolo, T. Chalklen, V. Narayan and S. Kar-Narayan, *ACS Appl. Mater. Interfaces*, 2018, **10**, 19580–19587.

48 A. D. Taylor, E. Y. Kim, V. P. Humes, J. Kizuka and L. T. Thompson, *J. Power Sources*, 2007, **171**, 101–106.

49 K. V. Wong and A. Hernandez, *ISRN Mech. Eng.*, 2012, **2012**, 1–10.

50 S. H. Jeong, K. Hjort and Z. Wu, *Sci. Rep.*, 2015, **5**, 8419.

51 O. Roslyak and A. Piryatinski, *J. Appl. Phys.*, 2016, **119**, 125107.

52 H. Wang, Y. Pei, A. D. Lalonde and G. J. Snyder, *Adv. Mater.*, 2011, **23**, 1366–1370.

53 J. Y. Lee, S. T. Connor, Y. Cui and P. Peumans, *Nano Lett.*, 2008, **8**, 689–692.

54 J. Choi, Y. Jung, S. J. Yang, J. Y. Oh, J. Oh, K. Jo, J. G. Son, S. E. Moon, C. R. Park and H. Kim, *ACS Nano*, 2017, **11**, 7608–7614.

55 L. Francioso, C. De Pascali, I. Farella, C. Martucci, P. Creti, P. Siciliano and A. Perrone, *Proc. IEEE Sensors*, 2010, **196**, 747–750.

56 S. Shin, R. Kumar, J. W. Roh, D. S. Ko, H. S. Kim, S. Il Kim, L. Yin, S. M. Schlossberg, S. Cui, J. M. You, S. Kwon, J. Zheng, J. Wang and R. Chen, *Sci. Rep.*, 2017, **7**, 1–9.

57 C. Y. Jiang, X. W. Sun, K. W. Tan, G. Q. Lo, A. K. K. Kyaw and D. L. Kwong, *Appl. Phys. Lett.*, 2008, **92**, 90–93.

58 M. Law, L. E. Greene, J. C. Johnson, R. Saykally and P. Yang, *Nat. Mater.*, 2005, **4**, 455–459.

59 J. Zhao, H. Li, C. Li, Q. Zhang, J. Sun, X. Wang, J. Guo, L. Xie, J. Xie, B. He, Z. Zhou, C. Lu, W. Lu, G. Zhu and Y. Yao, *Nano Energy*, 2018, **45**, 420–431.

60 N. Cui, J. Liu, L. Gu, S. Bai, X. Chen and Y. Qin, *ACS Appl. Mater. Interfaces*, 2015, **7**, 18225–18230.

61 S. Gong, W. Schwalb, Y. Wang, Y. Chen, Y. Tang, J. Si, B. Shirinzadeh and W. Cheng, *Nat. Commun.*, 2014, **5**, 1–8.

62 S. R. Das, Q. Nian, A. A. Cargill, J. A. Hondred, S. Ding, M. Saei, G. J. Cheng and J. C. Claussen, *Nanoscale*, 2016, **8**, 15870–15879.

63 J. Kim, R. Kumar, A. J. Bandodkar and J. Wang, *Adv. Electron. Mater.*, 2017, **3**, 1–15.

64 J. R. Sempionatto, R. K. Mishra, A. Martín, G. Tang, T. Nakagawa, X. Lu, A. S. Campbell, K. M. Lyu and J. Wang, *ACS Sensors*, 2017, **2**, 1531–1538.

CHAPTER 4. FULLY-PACKAGED CARBON NANOTUBE SUPERCAPACITORS BY DIRECT INK WRITING ON FLEXIBLE SUBSTRATES

This chapter is modified from a paper published in "Nanoscale, 2019, 11, 5222-5230"

Bolin Chen[1], Yizhou Jiang[2], Xiaohui Tang[1], and Yayue Pan[2,*], Shan Hu[1,*]

[1]Department of Mechanical Engineering, Iowa State University, IA, 50011, USA

[2]Department of Mechanical and Industrial Engineering, University of Illinois Chicago, IL, 60607, USA

*Corresponding authors: Shan Hu (shanhu@iastate.edu), Yayue Pan (yayuepan@uic.edu)

4.1 Abstract

The ability to print fully-packaged integrated energy storage components (e.g. supercapacitors) is of critical importance for the practical application of printed electronics. Due to the limited variety of printable materials, most studies on printed supercapacitors focus on printing the electrode materials but rarely the full-packaged cell. Herein, this work presented for the first time, the printing of a fully-packaged single-wall carbon nanotube based supercapacitors with direct ink writing (DIW) technology. Enabled by the developed ink formula, DIW setup, and cell architecture, the whole printing process is mask-free, transfer-free, and alignment-free with precise and repeatable control on the spatial distribution of all constituent materials. Studies on cell design shows that wider electrode pattern and narrower gap distance between electrodes lead to higher specific capacitance. The as-printed fully-packaged supercapacitors have energy and power performances that are among the best in recently reported planar carbon-based supercapacitors that are only partially-printed or non-printed.

4.2 Introduction

Printed electronics offer the promise of low cost, rapid prototyping, easy customization, and even flexible and conformal devices when printed on soft substrates. Printed electronic components have been extensively studied, such as transistors[1,2], sensors[3], displays[4], etc. Since power supply is an indispensable component of any electronics, to fully realize the promise of printed electronics, printed power sources have to be developed. Recently, supercapacitors have emerged as a promising energy storage device, due to its high power, long cycle life, and its ability to bridge the energy and power gap between batteries and conventional dielectric capacitors. Supercapacitors are widely used in electronic systems where fast and frequent charging/discharging is required. Hybrid power sources integrating batteries and supercapacitors together provide both high energy and high power at the same time.

A fully-packaged supercapacitor consists of integrated functional parts and structural parts. Functional parts are components that contribute directly to the energy storage, including electrode, electrolyte, and separator. While structural parts are those that do not store energy but are necessary for achieving stable performances, including sealed casing, support substrates, etc. Since each component is made of very different materials, printing a fully-packaged supercapacitor is challenging but necessary for practical application of printed supercapacitors.

Additive Manufacturing (AM), also known as 3D Printing or Direct Digital Manufacturing, is a class of technologies that fabricate a three-dimensional physical model directly from its digital design, by accumulating materials, usually in a layer-by-layer way. Considering the unique strengths such as maskless, one-step operation, and little material waste, AM technologies such as Fused Deposition Modeling (FDM), Inkjet Printing, and Direct Ink Writing (DIW) have been widely investigated for printed electronics in the past decade [5–14]. The major drawback of inkjet printing is the limited variety of printable materials: materials need to

have both flowability and jettability, which means only low-viscosity materials can be processed in this technique. The major disadvantage of FDM is that its printing resolution is low, usually in the range of 50~200 μm. In addition, the feedstocks have to be filaments that can be melted in a low temperature (<200 ºC). Compared with the Inkjet Printing and FDM technologies, the DIW technology has much wider choice of feedstocks ranging from highly viscous polymer gels to highly shear thinning colloidal suspensions, which allows an unrivaled freedom for choosing and preparing proper inks for the multi-material supercapacitor design. DIW method has demonstrated the capability of producing highly accurate, repeatable, and complex microstructures of any shape from a wide choice of materials in room temperatures, directly from digital design without the use of any masters or masks[15–18].

So far, most studies on printed supercapacitors focus on printing the electrode materials but rarely the fully-packaged cell. The printed electrodes are later assembled with other non-printed components. For example, Xie et al. used laser to pattern graphene/nickel electrodes on poly(ethylene terephthalate) (PET) film and later manually casted polyvinyl alcohol/lithium chloride gel electrolyte onto the electrodes and sealed the cell with PET by hot-melt glue[19]. Wang et al. used a commercial inkjet printer to pattern multi-wall carbon nanotube based nanocomposite electrodes on paper and later sandwiched the two electrodes with an electrolyte-soaked separator in between. Finally, they used adhesive tape to seal the cell[20]. Tehrani et al. used a screen presser and a series of masks to print carbon-silver electrodes, gel electrolyte, adhesives, and finally assembled two electrolyte loaded electrodes into a sealed cell with adhesives[21]. Although excellent electrochemical performances have been reported from these studies, the printing/patterning techniques used in these studies (laser processing, ink-jet printing, screen-printing) involve multiple aligning, transferring, and assembling steps to finally produce a

fully-packaged supercapacitor. These intermediate steps add uncertainties to the volume, mass, and performances of the as-made supercapacitors and decrease repeatability, which is very important for practical manufacturing.

Herein, we report for the first time the use of DIW technology for printing fully-packaged flexible supercapacitors. All components of the supercapacitor are directly written on a flexible polyimide substrate, including single-wall carbon nanotube (SW-CNT) electrode, polyvinyl alcohol (PVA) based gel electrolyte, and silicone for cell packaging and sealing. Single-wall carbon nanotube (SW-CNT) is used as the model electrode material in this study because it has high electrical conductivity, mechanical strength, as well as high specific surface area that is open to surface functionalization for enhanced energy storage performance. PVA can form flexible and quasi-solid-state electrolyte when mixed with a variety of aqueous electrolyte solution, such as sulfuric acid (H_2SO_4), phosphoric acid (H_3PO_4), lithium chloride (LiCl), potassium hydroxide, etc. Here, PVA-LiCl system is chosen as the model electrolyte for its neutral and benign nature. The entire printing process is assembly-free, transfer-free, and mask-free. DIW controls the spatial distribution of printed materials with high accuracy and repeatability, which is demonstrated by the printing of multiple highly symmetric supercapacitor connected in series.

4.3 Experimental Section

4.3.1 Preparation of Carbon Nanotube Ink and Polymer Gel Electrolyte Ink

High purity and large surface area SW-CNT (purity >95%, specific surface area >1075 $m^2\ g^{-1}$) is purchased from Timesnano (product code: TNSAR, Chengdu, China) and used as received. 32mg SW-CNT and 120 mg sodium n-dodecyl sulfate surfactant (SDS, Sigma Aldrich, USA) are added into 40 ml deionized (DI) water, and stirred at 300 rpm using magnetic stirring bar for 5 minutes. The mixture is then placed inside an ice-water bath and subjected to 10

minutes of probe sonication (QSonica Q500, 50% power) to disperse SW-CNT uniformly in the DI water. To prepare PVA-based gel electrolyte, 6g of PVA powder (Mowiol® 18-88, Sigma Aldrich, USA) and 12g of lithium chloride powder (>99.0%, Sigma Aldrich, USA) are added to 40 ml of DI water and stirred on a 85ºC hot plate until the mixture became a clear and glue-like gel. Silicone rubber is purchased from Nanda 705 RTV Silicon Rubber (Liyang, China) and used as received.

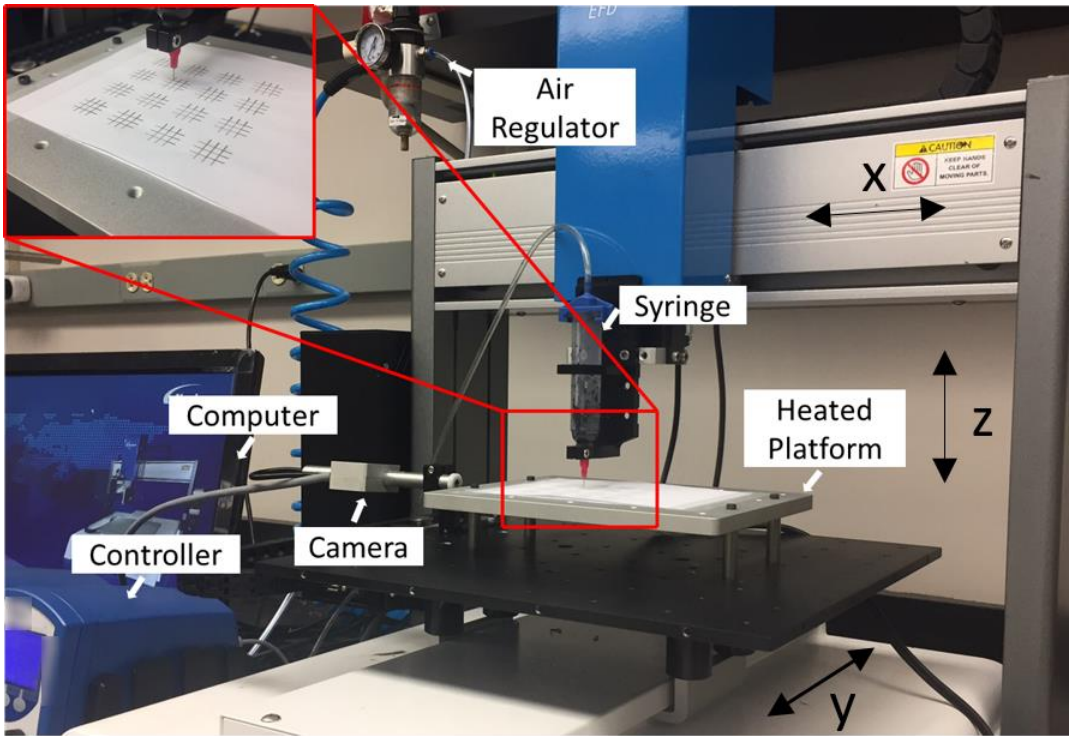

Figure 1. Photograph of the developed direct writing testbed.

4.3.2 Direct ink writing setup

In this study, a DIW testbed is developed to fabricate the fully-packaged supercapacitor, including electrode, electrolyte, and sealed package. DIW is achieved by dispensing inks through syringe needles in close proximity to a moving platform in a layer-by-layer way. As shown in Figure. 1, the testbed is equipped with a syringe needle, an air-pressure controller to regulate ink

dispensing rate, a heated platform, a charge coupled device (CCD) camera, an X-Z stage, and a Y stage. The syringe needle is mounted on an X-Z stage, and the platform is placed on a Y stage. The CCD camera is used to monitor the ink dispensing in real time and to measure the distance between tip and platform. The platform temperature is controlled and can be varied between 15 ~ 250 ^{o}C.

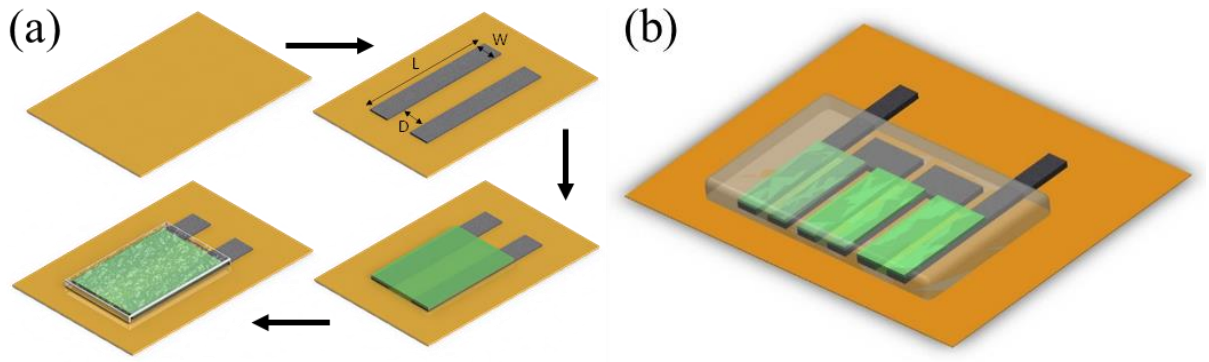

Scheme 1. (a) Schematic of layer design and printing process for DIW of the proposed supercapacitors. (b) An array of 3 identical cells connected in series

4.3.3 DIW of SW-CNT supercapacitor

The DIW process for rapid production of the proposed supercapacitor consists of four steps as illustrated in Scheme 1(a). During the entire printing process, the Kapton polyimide substrate (McMaster-Carr, USA) is fixed on the platform, which is controlled by the Y-stage. Firstly, 2ml SW-CNT ink is printed onto the Kapton substrate with a needle tip of 0.20mm inner diameter using 1.0 psi dispensing air pressure and 200mm/s writing speed (black region in Scheme 1(a)). With a platform temperature of 100 ^{o}C, the CNT solution is fully dried within 5 minutes. To remove surfactant and improve conductivity of the CNT electrode, the printed part is soaked in concentrated nitric acid for 20 minutes, quenched in DI water, and dried in air. Secondly, the dispensing tip moves up by 0.1 mm in the Z-direction to print the second layer. In the second layer, PVA electrolyte is then printed in the light green region in Scheme 1(a). To

print the PVA layer, a needle tip with 0.41 mm inner diameter is placed above the Kapton substrate with a 0.4 mm gap distance (also known as the standoff distance). The pumping pressure is set at 25 psi and the substrate speed is set at 5 mm/s in the Y-direction. Finally, a layer of silicone rubber is printed in the transparent region in Scheme 1(a). The needle tip (0.84 mm inner diameter) is placed above the Kapton film substrate with a ~0.6 mm standoff distance. A pumping pressure of 30 psi and a platform moving speed of 10 mm/s are used to print the silicone rubber layer. The silicone rubber layer covers the whole supercapacitor leaving only two SW-CNT electrode legs exposed for electrical connection.

To study how the electrode and electrolyte pattern design affect the overall performance of the supercapacitor, single-cell supercapacitor designs with different geometry are printed following the procedure given in Scheme 1(a). Specifically, the width of the electrode ("W" in Scheme 1(a)) and different distance between electrodes ("D" in Scheme 1(a)) are varied and their effects on the supercapacitor performances are compared. Multi-cell supercapacitor design is also printed. The design shown in Scheme 1(b) is an array of three identical supercapacitors connected in series.

4.3.4 Material and Electrochemical Characterization

The viscosity of the CNT ink, PVA electrolyte ink, and silicon rubber ink are measured by Malvern Kinexus ultra+ rheometer at 25 °C, with shear rate ranging from 1 to 100 s^{-1}. Microscopic image of the as-printed SW-CNT electrode is taken from FEI Quanta 250 FEG Scanning Electron Microscope (SEM) at an operating voltage of 10 kV. The XPS measurements of surface composition of the electrodes are performed using a Kratos Amicus/ESCA 3400 instrument. The sample is irradiated with 240 W unmonochromated Mg Kα x-rays, and photoelectrons emit at 0° from the surface normal are energy analyzed using a DuPont type

analyzer. The pass energy is set at 150 eV and either a Shirley or linear baseline is removed from all reported spectra. CasaXPS is used to process raw data files.

Galvanostatic charge-discharge (GCD), cyclic voltammetry (CV) and electrochemical impedance spectroscopy (EIS) are performed on the printed supercapacitors with Gamry Reference 3000 electrochemical station. The capacitances of each device at different current densities are calculated from the discharge curves obtained from GCD tests using the formula

$$C = I/\frac{\Delta U}{\Delta t} \quad (1)$$

Where I is the applied discharge current (amp), Δt is discharge time (second), ΔU (volt) is the discharge voltage after IR drop is removed.

The gravimetric, areal and volumetric specific capacitances of each device at different current densities are calculated from the discharge curves obtained from GCD tests using the following equations

$$C_{sp,g} = \frac{C}{m} \quad (2)$$

$$C_{sp,areal} = \frac{C}{A} \quad (3)$$

$$C_{sp,vol} = \frac{C}{V} \quad (4)$$

Where m (g), A (cm^2) and V (cm^3) are the mass, area and volume of the active materials of all electrodes. Here, active materials are the printed CNTs (dark grey region in Scheme 1) that overlap with the electrolyte (green region in Scheme 1).

As pointed out by Gogotsi and Simon et al., volumetric energy density and power density can provide more reliable performance metrics for porous nanomaterial based thin film devices compared to gravimetric capacitance.[22] As a result, the volumetric energy density (Wh cm^{-3}) of each device is calculated using

$$E = \frac{0.5 \times C \times \Delta U^2}{3600 \times V} \quad (5)$$

The volumetric power density (W cm^{-3}) of the device is calculated from

$$P = \frac{E}{\Delta t} \times 3600 \quad (6)$$

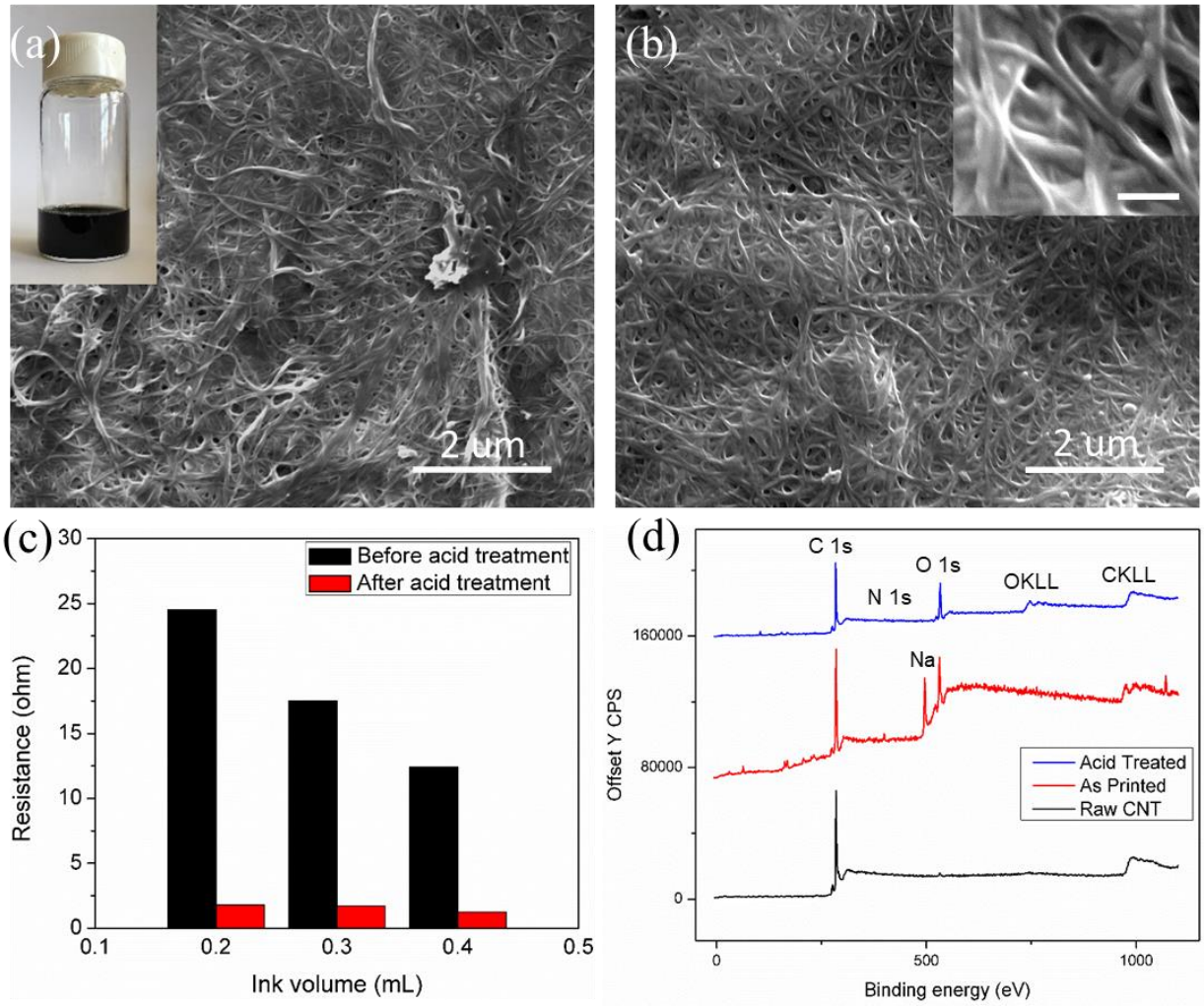

Figure 2. (a) SEM of as printed CNT electrode surface without acid-treatment; the inserted optical image shows the developed SW-CNT ink. (b) SEM of acid treated electrode surface with inserted high magnification image (scale bar 200 nm). (c) Change of resistance of printed traces with ink volume used before and after nitric acid treatment; (d) Full XPS spectrum of raw SW-CNT, as-printed SW-CNT without acid treatment, and with acid treatment.

4.4 Results and Discussion

The viscosity measurements of the inks for the SW-CNT electrode, PVA electrolyte, and silicone sealed package are plotted in Figure S1. The morphology of printed SW-CNT electrode before and after acid treatment are shown in Figure 2a-b. In as-printed electrodes, a layer of surfactant on top of the SW-CNT can be seen in Figure 2a. After acid treatment, the surfactant top layer seems to be removed and the highly porous structure of the SW-CNT can be clearly seen in Figure 2b. The inserted image in Figure 2a shows the prepared SW-CNT ink. Figure S2 shows the cross-section SEM of SW-CNT electrode with an average thickness of 1.26 μm. Different volumes of SW-CNT ink (0.2, 0.3, and 0.4 ml) are used to print traces 10 mm long and 3 mm wide. Resistances of traces with and without nitric acid treatment are measured and compared after the traces dry (Figure 2c). The resistance drops as the volume of ink used increases. The resistance drop at low ink volume is mainly explained by the percolation theory, which says that for nanotube and nanowire type materials to form a conductive 2D thin film, the nanotubes/nanowires must form a connected network[23,24]. When the volume of CNT ink used is still low, a continuous connected network of CNT has not formed yet across the whole electrode area and the reduction in electrode resistance with more ink is mainly ascribed to the gradual buildup of such a percolated network. With high ink volume, the deposited CNTs are more than enough to form a percolated network. Hence, the resistance drop is mainly due to increase of electrode thickness (*t*), following the Ohm's law $R_{CNT} = \rho_{CNT} Wt/l$, where W is the width of the electrode and l is the length of the electrode. After nitric acid treatment, the resistance of the electrode traces all drop compared with untreated ones. The full range XPS of printed SW-CNT with/without acid treatment are compared in Figure 2d, with the XPS of raw SW-CNT added as a reference. The high sodium (Na) contents in the SW-CNT without acid treatment comes from the Na of the SDS surfactant used for preparing the SW-CNT printing ink. More importantly,

after acid treatment, no sodium (Na) Auger (~495 eV) signal is detected, which suggests the significant removal of the SDS surfactant. Removing the highly-insulating SDS surfactant improves the electrical contact of nearby nanotube bundles and reduces the overall electrical resistance of SW-CNT electrodes.[25] High resolution XPS of the C1s, O1s and N1s of the raw SW-CNT and the printed SW-CNT electrode with and without acid treatment are shown in Figure S3-5. Compared with the C1s of the raw SW-CNT and the as-printed SW-CNT without acid treatment, there is a 0.3eV upshift of the C1s binding energy after acid treatment, indicating the oxidation of SW-CNT electrode by the nitric acid.[26] The O1s peak (531.2 eV) in as-printed SW-CNT electrode without acid treatment is attributed to the oxygen from the sulfate (SO_4^-) groups in the SDS surfactant.[27] In acid-treated samples, the O1s peak is shifted to 534.2 eV, which is attributed to the oxidation of SW-CNT by nitric acid.[28] The N1s peak (399.1 eV) in as-printed electrode without acid treatment is attributed to C-N bonding with pyridinic N, and the N1s peak (401.7 eV) in acid-treated sample is attributed to C-N bonding with quaternary N.[29] In summary, the XPS analysis confirms the two effects of acid treatment on the as-printed SW-CNT: (1) it significantly removes the SDS surfactant, which is the main reason for the reduced electrical resistance of the SW-CNT electrode after acid treatment; and (2) it partially oxidizes the SW-CNT, which can improve the contact between SW-CNT electrode and PVA hydrogel electrolyte [30,31].

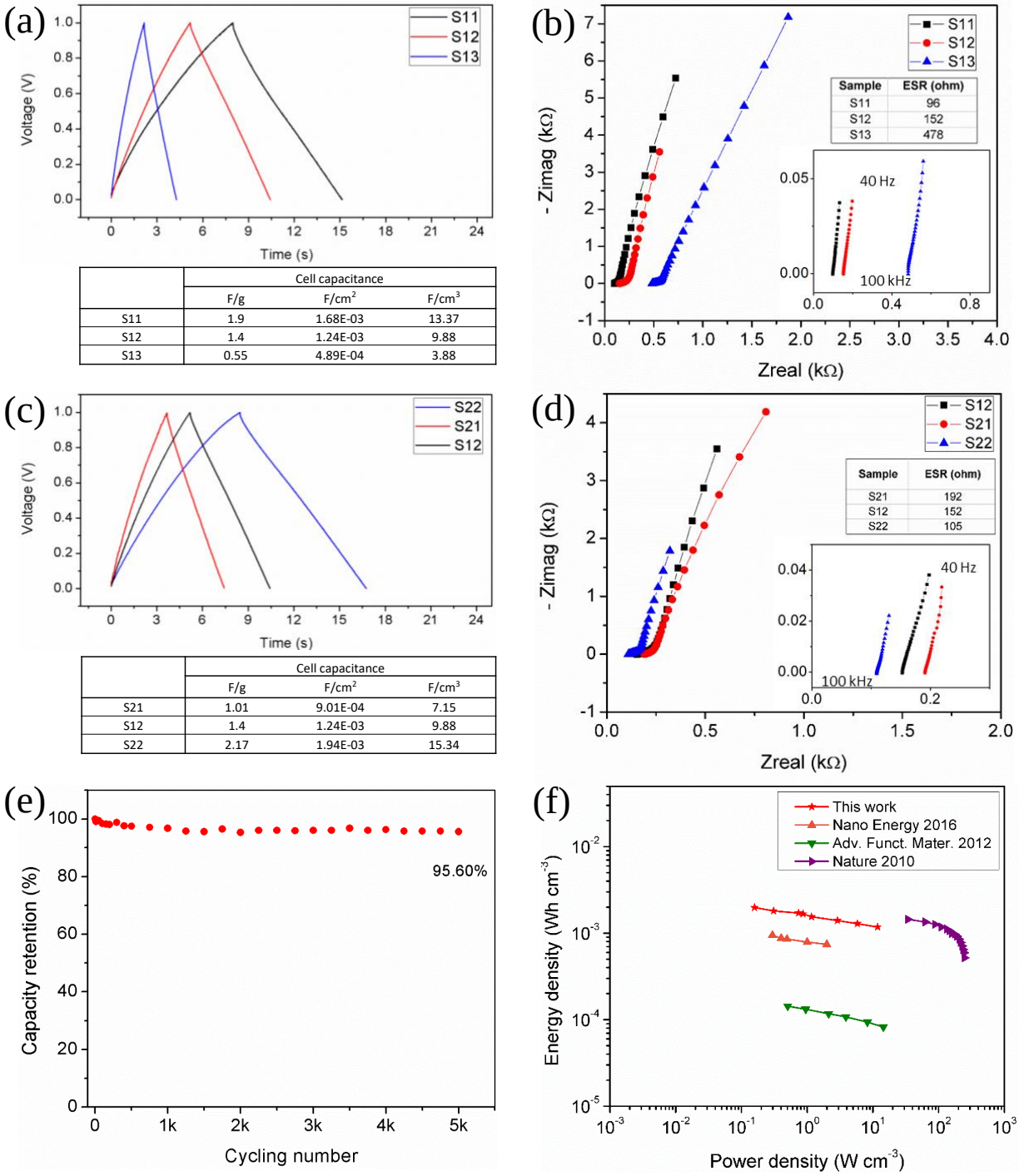

	Cell capacitance		
	F/g	F/cm^2	F/cm^3
S11	1.9	1.68E-03	13.37
S12	1.4	1.24E-03	9.88
S13	0.55	4.89E-04	3.88

	Cell capacitance		
	F/g	F/cm^2	F/cm^3
S21	1.01	9.01E-04	7.15
S12	1.4	1.24E-03	9.88
S22	2.17	1.94E-03	15.34

Figure 3. (a) Galvanostatic charge/discharge at 1.32 A cm^{-3} for cells in Study 1 and calculated specific capacitance and cell capacitance. (b) Nyquist plot of Study 1 supercapacitors from potentiostat EIS with inserted zoom-in at high frequency range and table of ESR values. (c) Galvanostatic charge/discharge at 1.32 A cm^{-3} for cells Study 2 and calculated specific capacitance

and cell capacitance. (d) Nyquist plot of Study 2 supercapacitors from potentiostat EIS with inserted zoom-in at high frequency range and table of ESR values. (e) 5000 cycles GCD of cell S22 at 1.32 A cm^{-3}. (f) Ragone plot of cell S22 compared with recent relevant work.

Table 1. Geometries used in electrode and electrolyte design studies.

Geometries*	Study 1			Study 2		
	S11	S12	S13	S21	S12	S22
Width or W (cm)	0.2			0.15	0.2	0.25
Length or L (cm)	2			2		
Gap Distance or D (cm)	0.1	0.2	0.4	0.2		

*Refer to Scheme 1a for how width (W), length (L) and gap distance (D) are defined.

Two studies on how electrode and electrolyte pattern design of the supercapacitor affect its electrochemical performance have been carried out. In the first study, we study the effect of the gap distance between two electrodes ("D" in Scheme 1(a)). Three fully-packaged supercapacitors with the same electrode geometry (i.e. width and height) are printed but with different gap distances at 1 mm, 2 mm, and 4 mm, thereafter referred as S11, S12, and S13 respectively. The exact geometry of the cells can be found in Table 1. The volume of SW-CNT ink is adjusted so that the density and thickness of SW-CNT is kept the same for S11, S12, and S13. To evaluate the electrochemical performance of the printed supercapacitors, galvanostatic charge-discharge (GCD), potentiostat EIS and cyclic voltammetry (CV) are performed at different conditions. The GCD curves of S11-S13 between 0-1 V at a current density of 1.32 A cm-3 and the calculated specific capacitance are shown in Figure 3a. All GCD curves have symmetric charge and discharge profiles, however it is obvious that S11 with the smallest electrode-gap distance of 1 mm has the highest specific capacitance of 13.37 F cm-3 (1.9F g-1

and 1.68 mF cm-2) followed by S12 and S13. There is a clear decreasing trend for the specific capacitance as the electrode-gap distance increases. The reason for this observed trend could be understood from the EIS of the three supercapacitors (Figure 3b). The Nyquist plots are almost-vertical straight lines at low frequencies, characteristic of capacitive behaviors.32–34 Intersect of the Nyquist plot with the real axis at high frequency is the equivalent series resistance (ESR) of the supercapacitor, which consists of resistances from both the electrode and electrolyte. Large ESR will cause large drop of voltage at the beginning of discharge, which decreases the usable discharge voltage window and capacity of the supercapacitor. As shown in Figure 3b, as the electrode-gap distance is increasing, the ESR increases from 95 ohms for S11 to 478 ohms for S13, mainly caused by the increased electrolyte resistance since the electrodes in all three cells are identical. The larger electrolyte resistance in S13 is caused by the larger electrode gap as explained in Table S1 and associated discussion in the Supporting Information. In short, for planar supercapacitors the electrolyte resistance (Rs) can be expressed as $R_s = \rho\kappa$, where ρ is the resistivity of the electrolyte and κ is the cell constant. As the gap distance increases, the cell constant also increases leading to higher electrolyte resistance Rs and degraded capacitive performance.35 From this study, it can be concluded that reducing the electrode-gap distance can enhance the capacitance of the as-printed supercapacitor. However, the printing resolution of DIW with the developed CNT ink limits how small the gap distance can be. Printing extra small gap distance beyond the resolution of DIW may lead to partial overlapping of two adjacent electrodes and the shorting of the two electrodes, which results in a completely malfunctioned device.

In the second study, the electrode-gap distance (“D” in Scheme 1a) and the height of the electrode pattern (“L” in Scheme 1a) are kept the same but the width of the electrode pattern

("W" in Scheme 1a) is changed from 1.5 mm to 2 mm and 2.5 mm, thereafter denoted as S21, S12, S22 respectively. The exact geometry of the cells can be found in Table 1. The volume of SW-CNT ink is adjusted so that the density and thickness of SW-CNT is kept the same for S21, S12, and S22. Specifically, the GCD curves of S21, S12, S22 between 0-1 V at a current density of 1.32 A cm-3 and the calculated specific capacitance are shown in Figure 3c. It is found that the specific capacitance increases as the electrode width increases from S21 (7.15 F cm-3) to S22 (15.34 F cm-3). The Nyquist plots in Figure 3d show that the ESR decreases as the electrode width increases. Different from study 1, this change in ESR in study 2 is caused by the changes of both the electrode resistance and the electrolyte resistance as the electrode width changes. Obviously, wider electrode patterns can lower the electrode resistance and enhance the capacitance of the printed supercapacitors. In addition, increasing electrode width also leads to the decrease of electrolyte resistance for planar supercapacitors,35 according to the analysis presented in Table S1 and the associated discussion in the Supporting Information. It should be noted that for optimal supercapacitor performance, the electrode width should not be arbitrarily large. As shown in the simulated electric field near the planar electrodes in Figure S6, the electric field becomes weaker at locations away from the edge of the electrodes, and so as the electrostatic force driving the formation of electric double layers (EDL). Thus, the active materials away from the electrode edges do not contribute as much EDL capacitance as those near the edges and the overall specific capacitance is decreased. With relatively narrow width, the benefits of increasing electrode width (i.e. lower electrode and electrolyte resistance) will overshadow the effect of non-uniform electric field and the specific capacitance will increase with electrode width (as shown in our study 2 results). It is expected that with extra wide electrode, the effect of non-uniform electric field will eventually become more significant than

the benefits of wide electrode and the specific capacitance will start decreasing with the increase of electrode width.

Table 2. Performance comparison of Carbon based planar supercapacitor

Active material	Electrolyte	Technique	capacitance	Energy density	Power density	Year	Ref.
Graphene	LiCl/PVA	laser process	0.694 F cm^{-3}	0.98 mWh cm^{-3}	0.3 W cm^{-3}	2016	[19]
carbon onion	Et_4NBF_4/anhydrous propylene carbonate	Laser process	1.3 F cm^{-3}	1.5 mWh cm^{-3}	35 W cm^{-3}	2010	[36]
Graphene	H_3PO_4/PVA	Inkjet printing	99 µ F cm^{-2}	N/A	N/A	2017	[37]
Reduced Graphene	H_2SO_4/PVA	MEMS	17.9 F cm^{-3}	2.5 mWh cm^{-3}	495 W cm^{-3}	2013	[32]
CNT	KCl	MEMS	6.1 F cm^{-3}	0.15 mWh cm^{-3}	0.3 W cm^{-3}	2012	[38]
Carbonized polyimide	H_2SO_4/PVA	laser process	42.6 mF cm^{-2}	N/A	N/A	2017	[39]
Carbon nanotube	LiCl/PVA	DIW	15.34 F cm^{-3}	1.2 mWh cm^{-3}	11.8 W cm^{-3}	2017	This Work

Cell S22 with the highest specific capacitance is used for further studies. Cyclic stability study (Figure 3e) showed that S22 can maintain ~96.5% of its initial capacitance after 5000 cycles of GCD at 1.32 A cm^{-3}. The energy density and power density of cell S22 are calculated using equation (5) and (6) at varied current density from 0.02 A cm^{-3} to 20 A cm^{-3} and compared with recent planar carbon based electric double layer capacitors (EDLCs) on Figure 3f. The S22 cell has a high energy density of 1.18 mWh cm^{-3} at power density of 11.8 W cm^{-3}. The energy and power performance of the as-printed fully-packaged supercapacitor is among the best in recently reported planar electric double layer capacitors and even higher than some graphene based supercapacitors (Table 2), which involved high cost fabrication process such as lithography patterning and high temperature annealing.

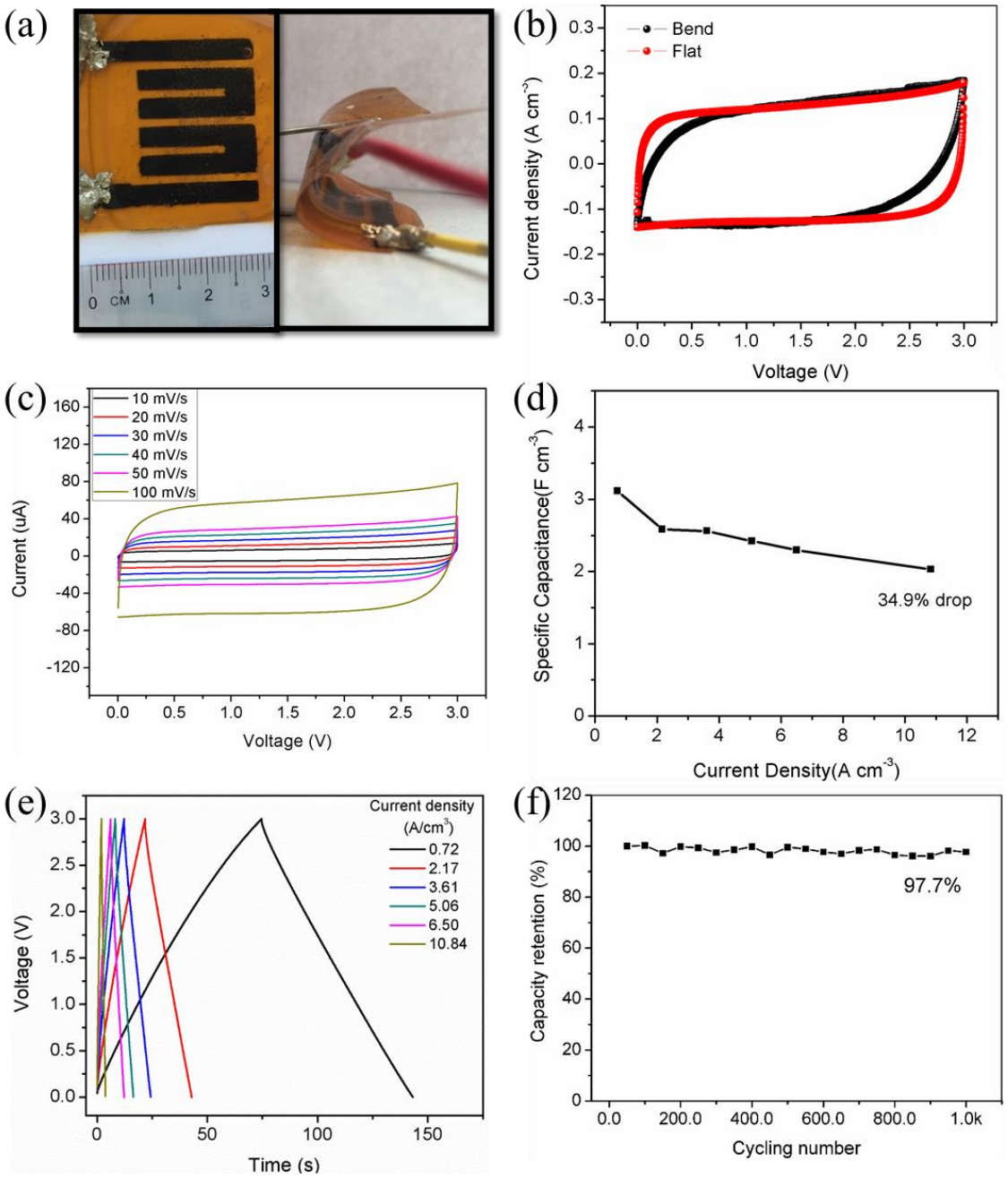

Figure 4. (a) Optical picture of the as-printed 3-cell supercapacitor array; 160° bended supercapacitor array; (b) CV comparison of bent and flat cells; (c) CV profiles of 3-cell supercapacitor at different scan rates; (d) Calculated specific capacitance at different current density; (e) Galvanostatic charge/discharge of 3-cell supercapacitor at varied current densities; (f) Cyclic performance of 3-cell supercapacitor at a constant 5.06 A cm^{-3} current density GCD.

An array of three supercapacitors connected in series is printed. Picture of the printed supercapacitor array is shown in Figure 4a. The SW-CNT electrode can be clearly seen in the picture, whereas the transparent electrolyte and silicone seal cannot be discerned in the picture. The supercapacitor is connected to electrical wires by silver paste. Since all components including the electrodes, the electrolyte, the substrate, and the seal are flexible, the as-printed supercapacitor showed excellent flexibility. CV test is performed when the cell is bent and the bent cell retains similar performance compare to unbent flat cell (Figure 4b), which proves the mechanical flexibility of the cell.

A series of CV tests is performed with a potential window of 0-3 V and varied scan rates of 10, 20, 30, 40, 50, and 100 mV s^{-1}. The CV curves (Figure 4c) all have rectangle shapes, which confirms the printed device is a pure electric double layer capacitor. The GCD curves measured at current densities 0.72, 2.17, 3.61, 5.06, 6.50, 10.84 A cm^{-3} are shown in Figure 4e. The charge and discharge curves are highly symmetric. Specific capacitances of the supercapacitor array are calculated by equation (1) and plotted at different current densities (Figure 4d). The specific capacitance only drops by 34.9 % when current density increases from 0.72 A cm^{-3} to 10.84 A cm^{-3} demonstrating good rate capability.

The cyclic stability is investigated by performing GCD at a current density of 5.06 A cm^{-3} (Figure 4f). There is no significant decrease of cell capacitance (~2.42 F cm^{-3}) and the capacitance is retained 97.7 % after 1000 cycles of charge/discharge. It is noted that the capacitance increases after a few cycles at the beginning of the cyclic test. This increase can be attributed to the increase of SW-CNT surface area induced by the surface activation effect of the charge/discharge process.

4.5 Conclusion

In this study, we report for the first time the direct ink writing (DIW) of fully-packaged supercapacitors on flexible polymer substrate. Different supercapacitor designs have been implemented by the DIW and electrochemical study results show that smaller gap spacing between two electrodes and wider electrode facilitate the fast ion transport and electron transport respectively, which improve the overall cell performance. A multi-cell supercapacitor array with three identical cells connected in series is printed to demonstrate the scalability of the developed technology. The direct-written fully-packaged SW-CNT supercapacitor has comparable energy and power performances to recently reported planer carbon-based supercapacitors fabricated by other printing or non-printing methods. The developed ink formula and direct ink writing setup enable the mask-free, transfer-free, and alignment-free printing with precise and repeatable control on the spatial distribution of different functional materials. It paves the way for rapid, low cost, and scalable manufacturing of high performance fully-packaged supercapacitors for practical applications.

4.6 References

(1) Homenick, C. M.; James, R.; Lopinski, G. P.; Dunford, J.; Sun, J.; Park, H.; Jung, Y.; Cho, G.; Malenfant, P. R. L. Fully Printed and Encapsulated SWCNT-Based Thin Film Transistors via a Combination of R2R Gravure and Inkjet Printing. *ACS Appl. Mater. Interfaces* **2016**, *8*, 27900–27910.

(2) Medina-Sánchez, M.; Martínez-Domingo, C.; Ramon, E.; Merkoçi, A. An Inkjet-Printed Field-Effect Transistor for Label-Free Biosensing. *Adv. Funct. Mater.* **2014**, *24*, 6291–6302.

(3) Kulkarni, M. V; Apte, S. K.; Naik, S. D.; Ambekar, J. D.; Kale, B. B. Ink-Jet Printed Conducting Polyaniline Based Flexible Humidity Sensor. *Sensors Actuators B Chem.* **2013**, *178*, 140–143.

(4) Lindh, E. M.; Sandström, A.; Edman, L. Inkjet Printed Bilayer Light-Emitting Electrochemical Cells for Display and Lighting Applications. *Small* **2014**, *10*, 4148–4153.

(5) Zhou, N.; Liu, C.; Lewis, J. A.; Ham, D. Gigahertz Electromagnetic Structures via Direct Ink Writing for Radio-Frequency Oscillator and Transmitter Applications. *Adv. Mater.* **2017**, *29*, 1605198--n/a.

(6) Malone, E.; Rasa, K.; Cohen, D.; Isaacson, T.; Lashley, H.; Lipson, H. Freeform Fabrication of Zinc-Air Batteries and Electromechanical Assemblies. *Rapid Prototyp. J.* **2004**, *10*, 58–69.

(7) Kim, Y. H.; Yoo, B.; Anthony, J. E.; Park, S. K. Controlled Deposition of a High-Performance Small-Molecule Organic Single-Crystal Transistor Array by Direct Ink-Jet Printing. *Adv. Mater.* **2012**, *24*, 497–502.

(8) Liu, Y.; Cui, T.; Varahramyan, K. All-Polymer Capacitor Fabricated with Inkjet Printing Technique. *Solid. State. Electron.* **2003**, *47*, 1543–1548.

(9) Liu, N.; Zhou, Y.; Ai, N.; Luo, C.; Peng, J.; Wang, J.; Pei, J.; Cao, Y. High-Performance, All-Solution-Processed Organic Nanowire Transistor Arrays with Inkjet-Printing Patterned Electrodes. *Langmuir* **2011**, *27*, 14710–14715.

(10) Sirringhaus, H.; Kawase, T.; Friend, R. H.; Shimoda, T.; Inbasekaran, M.; Wu, W.; Woo, E. P. High-Resolution Inkjet Printing of All-Polymer Transistor Circuits. *Science (80-.).* **2000**, *290*, 2123–2126.

(11) Maynor, B. W.; Filocamo, S. F.; Grinstaff, M. W.; Liu, J. Direct-Writing of Polymer Nanostructures: Poly(thiophene) Nanowires on Semiconducting and Insulating Surfaces. *J. Am. Chem. Soc.* **2002**, *124*, 522–523.

(12) Muth, J. T.; Vogt, D. M.; Truby, R. L.; Meng????, Y.; Kolesky, D. B.; Wood, R. J.; Lewis, J. A. Embedded 3D Printing of Strain Sensors within Highly Stretchable Elastomers. *Adv. Mater.* **2014**, *26*, 6307–6312.

(13) Boley, J. W.; White, E. L.; Chiu, G. T. C.; Kramer, R. K. Direct Writing of Gallium-Indium Alloy for Stretchable Electronics. *Adv. Funct. Mater.* **2014**, *24*, 3501–3507.

(14) Wehner, M.; Truby, R. L.; Fitzgerald, D. J.; Mosadegh, B.; Whitesides, G. M.; Lewis, J. A.; Wood, R. J. An Integrated Design and Fabrication Strategy for Entirely Soft, Autonomous Robots. *Nature* **2016**, *536*, 451–455.

(15) Lewis, J. A. Direct Ink Writing of 3D Functional Materials. *Adv. Funct. Mater.* **2006**, *16*, 2193–2204.

(16) Lewis, J. A.; Smay, J. E.; Stuecker, J.; Cesarano, J. Direct Ink Writing of Three-Dimensional Ceramic Structures. *J. Am. Ceram. Soc.* **2006**, *89*, 3599–3609.

(17) Li, R.-Z.; Hu, A.; Zhang, T.; Oakes, K. D. Direct Writing on Paper of Foldable Capacitive Touch Pads with Silver Nanowire Inks. *ACS Appl. Mater. Interfaces* **2014**, *6*, 21721–21729.

(18) Wei, H.; Zhang, Q.; Yao, Y.; Liu, L.; Liu, Y.; Leng, J. Direct-Write Fabrication of 4D Active Shape-Changing Structures Based on a Shape Memory Polymer and Its Nanocomposite. *ACS Appl. Mater. Interfaces* **2017**, *9*, 876–883.

(19) Xie, B.; Wang, Y.; Lai, W.; Lin, W.; Lin, Z.; Zhang, Z.; Zou, P.; Xu, Y.; Zhou, S.; Yang, C.; *et al.* Laser-Processed Graphene Based Micro-Supercapacitors for Ultrathin, Rollable, Compact and Designable Energy Storage Components. *Nano Energy* **2016**, *26*, 276–285.

(20) Wang, S.; Liu, N.; Tao, J.; Yang, C.; Liu, W.; Shi, Y.; Wang, Y.; Su, J.; Li, L.; Gao, Y. Inkjet Printing of Conductive Patterns and Supercapacitors Using a Multi-Walled Carbon nanotube/Ag Nanoparticle Based Ink. *J. Mater. Chem. A* **2015**, *3*, 2407–2413.

(21) Tehrani, Z.; Thomas, D. J.; Korochkina, T.; Phillips, C. O.; Lupo, D.; Lehtimäki, S.; O'Mahony, J.; Gethin, D. T. Large-Area Printed Supercapacitor Technology for Low-Cost Domestic Green Energy Storage. *Energy* **2017**, *118*, 1313–1321.

(22) Gogotsi, Y.; Simon, P. True Performance Metrics in Electrochemical Energy Storage. *Science (80-.).* **2011**, *334*, 917–918.

(23) Hu, L.; Hecht, D. S.; Grüner, G. Percolation in Transparent and Conducting Carbon Nanotube Networks. *Nano Lett.* **2004**, *4*, 2513–2517.

(24) Pike, G. E.; Seager, C. H. Percolation and Conductivity: A Computer Study. I. *Phys. Rev. B* **1974**, *10*, 1421–1434.

(25) Geng, H.-Z.; Kang, K.; Kang, K.; So, P.; Lee, Y. S.; Chang, Y.; Lee, Y. H. Effect of Acid Treatment on Carbon Nanotube-Based Flexible Transparent Conducting Films.

(26) Kwon, J.-Y.; Kim, H.-D. Preparation and Properties of Acid-Treated Multiwalled Carbon Nanotube/waterborne Polyurethane Nanocomposites. *J. Appl. Polym. Sci.* **2005**, *96*, 595–604.

(27) Terlingen, J. G. A.; Feijen, J.; Hoffman, A. S. Immobilization of Surface Active Compounds on Polymer Supports Using Glow Discharge Processes. *J. Colloid Interface Sci.* **1993**, *155*, 55–65.

(28) Xie, Y.; Sherwood, P. M. A. E-35 Pitch-based Carbon Fiber by Core Level and Valence Band XPS. *Surf. Sci. Spectra* **1992**, *1*, 198–203.

(29) Daems, N.; Sheng, X.; Vankelecom, I. F. J.; Pescarmona, P. P. Metal-Free Doped Carbon Materials as Electrocatalysts for the Oxygen Reduction Reaction. *J. Mater. Chem. A* **2014**, *2*, 4085–4110.

(30) Tang, X.; Lui, Y. H.; Chen, B.; Hu, S. Functionalized Carbon Nanotube Based Hybrid Electrochemical Capacitors Using Neutral Bromide Redox-Active Electrolyte for Enhancing Energy Density. *J. Power Sources* **2017**, *352*, 118–126.

(31) Jin, H.; Wang, X.; Gu, Z.; Polin, J. Carbon Materials from High Ash Biochar for Supercapacitor and Improvement of Capacitance with HNO3 Surface Oxidation. *J. Power Sources* **2013**, *236*, 285–292.

(32) Wu, Z.; Parvez, K.; Feng, X.; Müllen, K. Graphene-Based in-Plane Micro-Supercapacitors with High Power and Energy Densities. *Nat. Commun.* **2013**, *4*.

(33) Sheng, K.; Sun, Y.; Li, C.; Yuan, W.; Shi, G. Ultrahigh-Rate Supercapacitors Based on Eletrochemically Reduced Graphene Oxide for Ac Line-Filtering. *Sci. Rep.* **2012**, *2*.

(34) Kötz, R.; Carlen, M. Principles and Applications of Electrochemical Capacitors. *Electrochim. Acta* **2000**, *45*, 2483–2498.

(35) Olthuis, W.; Streekstra, W.; Bergveld, P. Theoretical and Experimental Determination of Cell Constants of Planar-Interdigitated Electrolyte Conductivity Sensors. *Sensors Actuators B. Chem.* **1995**, *24*, 252–256.

(36) Pech, D.; Brunet, M.; Durou, H.; Huang, P.; Mochalin, V.; Gogotsi, Y.; Taberna, P.-L.; Simon, P. Ultrahigh-Power Micrometre-Sized Supercapacitors Based on Onion-like Carbon. *Nat. Nanotechnol.* **2010**, *5*, 651–654.

(37) Sollami Delekta, S.; Smith, A. D.; Li, J.; Ostling, M. Inkjet Printed Highly Transparent and Flexible Graphene Micro-Supercapacitors. *Nanoscale* **2017**, *9*, 6998–7005.

(38) Beidaghi, M.; Wang, C. Micro-Supercapacitors Based on Interdigital Electrodes of Reduced Graphene Oxide and Carbon Nanotube Composites with Ultrahigh Power Handling Performance. *Adv. Funct. Mater.* **2012**, *22*, 4501–4510.

(39) Wang, S.; Yu, Y.; Li, R.; Feng, G.; Wu, Z.; Compagnini, G.; Gulino, A.; Feng, Z.; Hu, A. High-Performance Stacked in-Plane Supercapacitors and Supercapacitor Array Fabricated by Femtosecond Laser 3D Direct Writing on Polyimide Sheets. *Electrochim. Acta* **2017**, *241*, 153–161.

CHAPTER 5. CONCLUSION

In this dissertation, the advantage of using additive manufacturing process such as direct ink writing and inkjet printing to fabricate various functional energy devices has been demonstrated. Printing is a versatile and cost-effective approach to deposit 2D or 1D nanomaterials that does not require cleanroom technology or masks/stencils that are typically associated with e-beam evaporation, sputtering, or screen-printing. The printed device shows good bending stability after intense bends. The developed technique can also be applied in other applications which requires a film like structure been deposited onto a substrate such as solar cells, biosensors, actuators.